

25. MILLENNIAL-SCALE COMPOSITIONAL VARIATIONS IN LATE QUATERNARY SEDIMENTS AT SITE 1017, SOUTHERN CALIFORNIA¹

Ryuji Tada,² Sohei Sato,² Tomohisa Irino,³ Hiroyuki Matsui,² and James P. Kennett⁴

ABSTRACT

Intensification of North Pacific Intermediate Water during the Younger Dryas and stadials of the last glacial episode has been advocated by Kennett and his colleagues based on studies of ventilation history in Santa Barbara Basin. Because Santa Barbara Basin is a semi-isolated marginal basin, this hypothesis requires testing in sequences on the upper continental margin facing the open-ocean of the Pacific.

Ocean Drilling Program Site 1017 is located on the upper slope of southern California off Point Conception close to the entrance of Santa Barbara Basin, an ideal location to test the hypothesis of late Quaternary switching in intermediate waters. We examined chemical and mineral composition, sedimentary structures, and grain size of hemipelagic sediments representing the last 80 k.y. at this site to detect changes in behavior of intermediate waters. We describe distinct compositional and textural variations that appear to reflect changes in grain size in response to flow velocity fluctuations of bottom waters. Qualitative estimates of changes in degree of pyritization indicate better ventilation of bottom water during intervals of stronger bottom-water flow. Comparison between variations in the sediment parameters and the planktonic $\delta^{18}\text{O}$ record indicates intensified bottom-current activity during the Younger Dryas and stadials of marine isotope Stage 3. This result strongly supports the hypothesis of Kennett and his colleagues.

Our investigation also suggests strong grain-size control on organic carbon content (and to less extent carbonate carbon content). This, in turn, suggests the possibility that organic carbon content of sediments, which is commonly used as an indicator of surface productivity, can be influenced by bottom currents.

INTRODUCTION

The California margin is marked by strong coastal upwelling and consequent development of intense oxygen-minimum zone (OMZ). The strength and width of OMZ is controlled not only by intensity of upwelling but by concentration of dissolved O_2 and lateral advection of intermediate water. At present, upwelling is most intense between 33° and 44°N , the position and intensity of which is sensitive to the pattern of atmospheric circulation over the California margin. A significantly different situation almost certainly prevailed during the last glacial episode (Lyle et al., 1992). At present, warm, nutrient-rich, and O_2 -poor intermediate water (California Undercurrent) from the south continues as far north as Vancouver Island ($\sim 50^\circ\text{N}$) with the northernmost extent of this influence controlled by the position of the West Wind Drift (Hickey, 1979). But probable influence of North Pacific Intermediate Water (NPIW) at the depth of OMZ today is also suggested, and possible intensification of NPIW during the last glacial episode is widely discussed (van Green et al., 1996; Lund and Mix, 1998; Gardner et al., 1997; Keigwin, 1998). Thus, changes in both atmospheric circulation pattern and source and intensity of intermediate waters should have strong influence on the OMZ.

In their studies of Santa Barbara Basin during the last glacial episode, Kennett and Ingram (1995) and Behl and Kennett (1996) recognized changes of bottom-water oxygenation level in association with millennial-scale climatic cycles known as Dansgaard-Oeschger cycles (e.g., Dansgaard et al., 1993). They attributed these changes to switching of the intermediate-water sources between the south and the north. If true, this is a good evidence that the intermediate-water

circulation cell, independent of the deep-water conveyor belt driven by North Atlantic Deep Water, was intensified and expanded in North Pacific during stadials of the last glacial episode (Gonopolski et al., 1998). This further suggests that such waxing and waning of NPIW occurred in association with Dansgaard-Oeschger cycles. However, it has not yet been confirmed whether bottom-water conditions of Santa Barbara Basin faithfully reflect those of the intermediate water flowing along the California margin. To test this hypothesis, we planned a cooperative high-resolution multiparameter study at Ocean Drilling Program (ODP) Site 1017 located on the upper slope facing to open northeastern Pacific near the entrance of Santa Barbara Basin. This paper reports a part of the result from this cooperative study. Parameters examined in associated papers include $\delta^{18}\text{O}$ and $\delta^{13}\text{C}$ of planktonic and benthic foraminifers, $\delta^{13}\text{C}$ and $\delta^{15}\text{N}$ of organic matter, redox-sensitive minor elements, and biomarkers (Kennett et al., Chap. 21, this volume; Irino and Pedersen, Chap. 23, this volume; Ishiwatari et al., Chap. 24, this volume; Behl et al., Chap. 22, this volume; Ostertag-Henning and Stax, Chap. 26, this volume). The synthesis of these results will be presented elsewhere.

In this study, we aim to test the possibility of the changes in flow direction and intensity of the intermediate waters through examination of detrital provenance and sedimentary structures in conjunction with detrital grain size, respectively.

STUDIED SITE

The studied site, ODP Site 1017 ($34^\circ 32'\text{N}$, $121^\circ 6'\text{W}$, water depth = 955.6 m), is located ~ 60 km to the west of Point Conception, on the upper part of the continental slope called the Santa Lucia Slope (Fig. 1). The Santa Lucia Slope faces southwest with its shallow end bounded by the Santa Lucia Bank. According to Hickey (1979), the present surface water at the site is under the influence of the California Current from the north and a northward branch of the Southern California Countercurrent from the southeast. The latter is continuous with the Davidson Current flowing from the south during winter

¹Lyle, M., Koizumi, I., Richter, C., and Moore, T.C., Jr. (Eds.), 2000. *Proc. ODP, Sci. Results, 167*: College Station TX (Ocean Drilling Program).

²Geological Institute, University of Tokyo, 7-3-1 Hongo, Tokyo 113-0033, Japan. ryuji@tsunami.geol.s.u-tokyo.ac.jp

³Department of Earth and Planetary Sciences, Hokkaido University, Kita-10, Nishi-8, Kitaku, Sapporo, 060-0810, Japan.

⁴Department of Geological Science and Marine Science Institute, University of California, Santa Barbara, Santa Barbara CA 93106, USA.

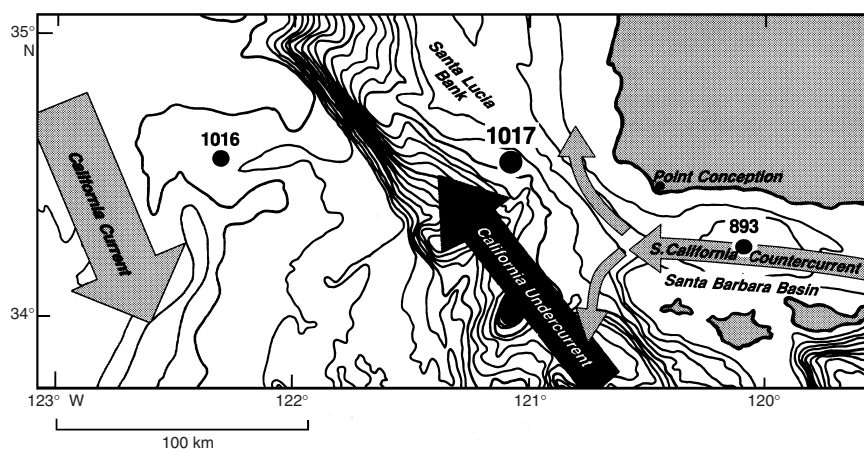


Figure 1. A map showing the locations of the studied site and related sites referred to in the text. Also schematically shown are present surface and subsurface current systems around this site.

when there is no upwelling. The present bottom water at this site is probably under the influence of California Undercurrent from the south, which is marked by high temperature, salinity, and phosphate, and low dissolved oxygen (Hickey, 1979). The core depth of the California Undercurrent off Point Conception is 200–300 m, but can be deeper than 500 m during spring (Hickey, 1979). Its flow speed is generally slow (<10 cm/s), but a maximum speed sometimes exceeds 22 cm/s. It is also possible that the bottom water is influenced by NPIW as discussed by van Green et al. (1996). The site is located within the lower part of present OMZ. This position is ideal to monitor changes in intensity and/or depth of the OMZ through time. The site is also close (~70 km northwest) to the entrance of Santa Barbara Basin, an ideal location to test the hypothesis that bottom-water oxygenation of Santa Barbara Basin has been driven by changes in intermediate water source in the North Pacific (Kennett and Ingram, 1995; Behl and Kennett, 1996).

STUDIED CORES AND AGES

Core Gap Estimation and Depth Correction

Cores 167-1017E-1H through 3H, which cover the top 24.9 m of the sediments, are dedicated for high-resolution study of late Quaternary paleoceanography of the California margin, and the top two of these are analyzed in this study. Recovery of the three cores was excellent, exceeding 100%. Immediately after cutting the cores into sections, the sections were tightly sealed and stored at -15°C for three months before sampling at Texas A&M University (TAMU). Correlation of gamma-ray attenuation porosity evaluator (GRAPE) and color profiles at Hole 1017E with those of other holes in conjunction with correlation of marker sand layers based on visual core descriptions (VCDs) was conducted to identify potential sediment loss at the core top and core gaps. Correlation with the other four holes suggests no significant sediment loss at the top of Core 167-1017E-1H. Details of core gap estimation and correction of meter below seafloor (mbsf) depths are described in Kennett et al. (Chap. 21, this volume).

Core Lithology

Visual Core Description

Lithology of the studied cores were described based on visual inspection at TAMU, where cores were split and sampled, supplemented by smear-slide observation afterwards. The studied cores are composed of grayish olive (5Y 4/2 to 4/3), homogeneous hemipelagic clayey silt to silty clay with occasional intercalations of grayish olive (5Y 3/1) medium- to fine-grained sand layers (Fig. 2). Burrows are difficult to identify visually except open burrows of 0.5–1 cm in diameter, which are present in the upper 1.5 m. Carbonaceous plant remains

occur at 2.3, 5.25, 10.4–11.2, 12.3–12.5, 13.4, and 13.9–14.0 mbsf, and shell fragments occur at 7.4 mbsf.

Sand layers are 1–3 cm thick, except one layer at 14.75 mbsf, which is 10 cm thick. Sand layers generally have sharp basal contacts, show normal size grading, and contain reworked microfossils and shell fragments, suggesting their turbidite origin. These sand layers are concentrated in two intervals. One is between 3.2 and 5.0 mbsf and the other is between 13.9 and 14.7 mbsf (Fig. 2), corresponding to marine isotope Stages (MIS) 2 and 4, respectively. Sand layers in MIS 2 generally contain bioclasts including foraminiferal skeletons. A sand layer at 5.07 mbsf is especially enriched in zircon, spinel, and other heavy minerals. On the other hand, a thick sand layer at 14.75 mbsf is characterized by abundant glauconite grains.

X-Ray Radiography

X-ray radiographs of the slab samples were taken using SOFTEX CMB-2 at voltage of 40 kV, current of 20 mA, and exposure time of 240 s to observe detailed sedimentary structures and fabrics. On X-ray radiographs, several types of burrows are recognized. *Chondrites*-like burrows that are ~1 mm in diameter, filled with less dense material (lighter color on X-ray radiographs), are heavily condensed to form a 1–10 cm thick zone (Fig. 3A). These *Chondrites*-like burrow zones are abundant in an interval between 0 and 1.0 mbsf, common in intervals between 1.0 and 2.0 mbsf and 4.0 and 5.3 mbsf, and also present at 11.6 mbsf (Fig. 2). Larger burrows that are as large as 1 cm in diameter and subparallel or oblique to stratification are also recognized occasionally (Fig. 3B) and schematically illustrated in the lithologic columns in Figure 2. These larger burrows occur in intervals between 0.0 and 2.8 mbsf, 7.9 and 10.3 mbsf, 11.6 and 12.5 mbsf, 13.4 and 13.6 mbsf, and 14.9 and 15.1 mbsf.

Other than these burrow intervals, clayey silt and silty clay show homogeneous to slightly mottled appearance on X-ray radiographs that may reflect intense bioturbation. These homogeneous to slightly mottled clayey silt to silty clay are further subdivided into three types based on their textures on X-ray radiographs. The first type includes those with abundant opaque filaments of less than 1 mm thick and as much as 3 cm long, which are oblique to stratification (Fig. 3C). Examination of the corresponding slab samples suggests that these filaments are composed of aggregates of framboidal pyrite. The matrix of this type generally shows transparent appearance on X-ray radiographs. The second type includes those with abundant disseminated submillimeter-size opaque particles, also considered to be framboidal pyrite (Fig. 3D). The matrix of this type exhibits a dusty appearance compared to the first type. The third type includes those without a significant amount of opaque particles or filaments, and its matrix is dusty compared to the first type (Fig. 3E). The first and second types alternate with the third type in decimeter scale below 1.5 mbsf.

The submillimeter-scale distinct parallel lamination characteristic of varves is not recognized on X-ray radiographs examined. How-

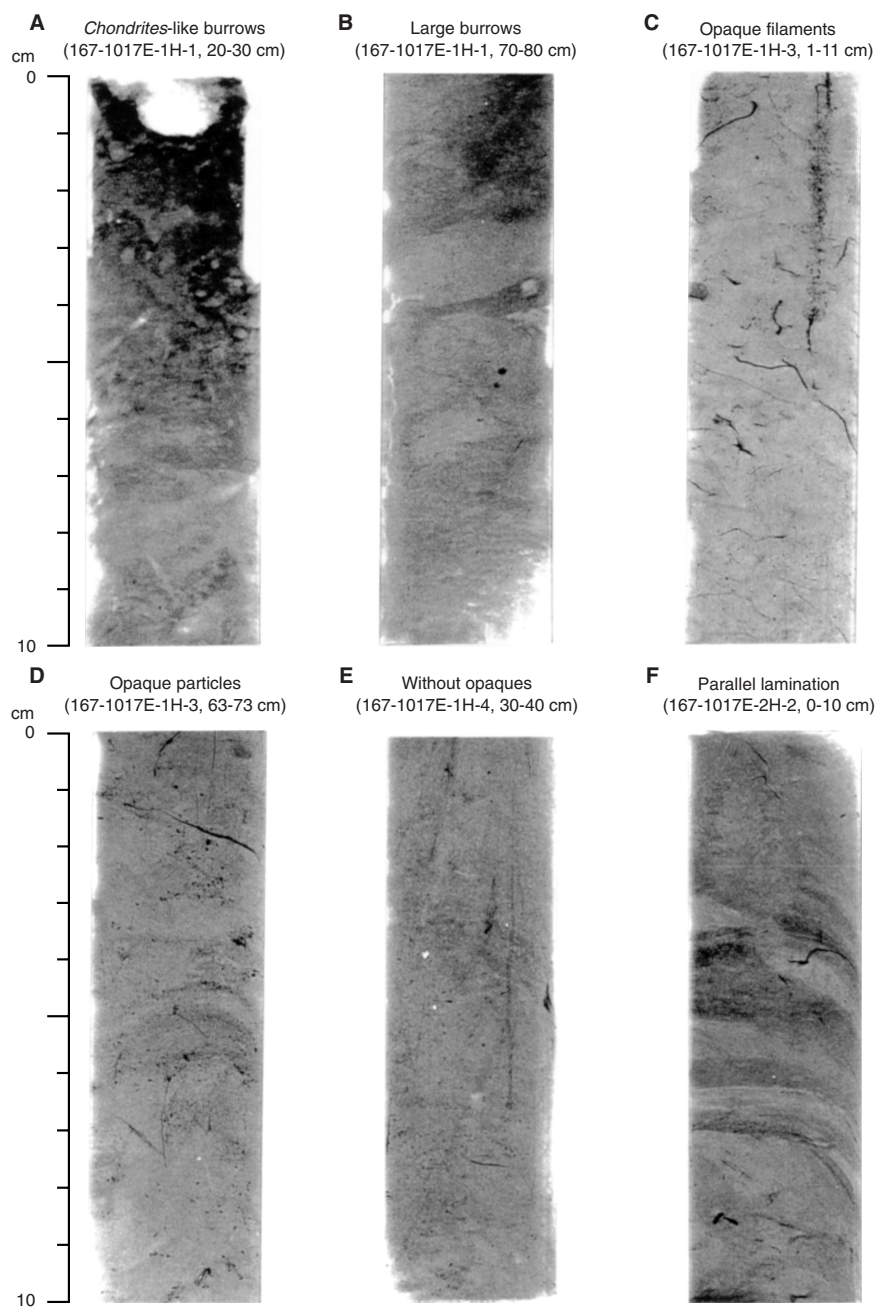


Figure 3. X-ray radiographs (positive) of six different sedimentary facies types of hemipelagic clayey silt to silty clay from Cores 167-1017E-1H and 2H. **A.** Chondrites-like burrows. **B.** Large burrows. **C.** Opaque filaments. **D.** Opaque particles. **E.** Without opaques. **F.** Parallel lamination. Names of each facies (except parallel lamination) correspond to those in the legend of Figure 2.

ever, millimeter-scale faint lamination is recognized at 3.2, 4.0, 5.2, 6.2, 7.4, 9.4, 10.0, 12.3, 14.1, and 14.6 mbsf (Fig. 3F), which occur within Type 3 homogeneous clayey silt to silty clay. In addition, sharp contacts of possible nondepositional surfaces are recognized at 2.55, 2.75, and 9.0 mbsf. These faint lamination and sharp contact surfaces are considered to be formed by winnowing of bottom current, as will be discussed later.

Age Model

An age model for Hole 1017E has been constructed by Kennett et al. (Chap. 21, this volume) based on AMS ^{14}C dates of mixed

planktonic foraminifers in the upper part and correlation of $\delta^{18}\text{O}$ profile of *Globigerina bulloides* from Hole 1017E with the $\delta^{18}\text{O}$ curve of Martinson et al. (1987) in the lower part of the sequence. We adopted their age model for the part younger than 82 ka (Fig. 4). Sediment ages between the datums are estimated by linear interpolation. Linear sedimentation rates during the last 82 k.y. range from 2.7 to 31 cm/k.y. Low linear sedimentation rates of 6.6 cm/k.y. and 2.7–6.9 cm/k.y. correspond to stratigraphic intervals between 2.74 and 2.89 mbsf (12.2–14.4 ka) and 12.24 and 12.85 mbsf (59.0–70.8 ka), respectively. These estimated low linear sedimentation rates are suggested by sediment features. We found a possible erosional surface approximately at 2.75 mbsf, which may represent a small hiatus

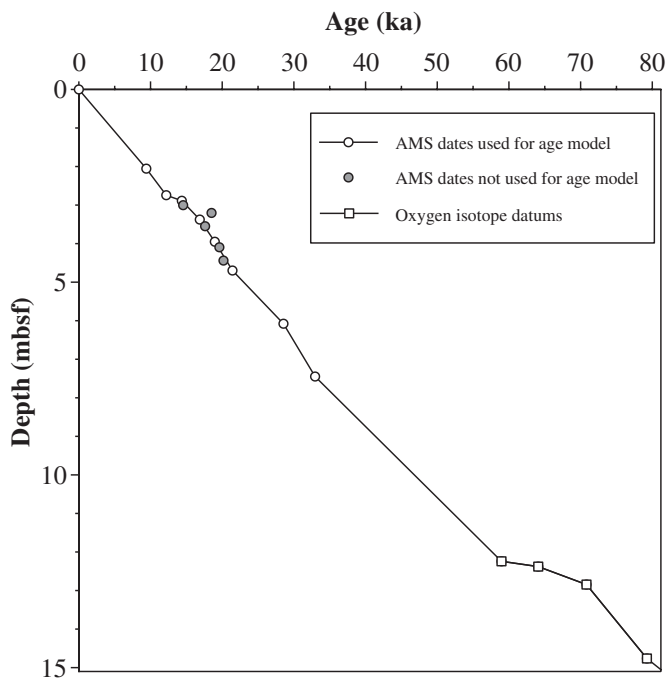


Figure 4. A diagram showing age-depth relation for the top 15 m of Hole 1017E based on age model of Kennett et al. (Chap. 21, this volume).

corresponding to the onset of the Younger Dryas, and a faintly laminated sandy interval between 12.4 and 12.2 mbsf, which may represent strong winnowing.

SAMPLING AND SAMPLE PREPARATION

Sampling was conducted at TAMU ~3 months after the cruise. Samples of ~20 cm³ in volume were taken from Cores 167-1017E-1H through 3H in 3-cm intervals. These samples were immediately placed in k-packs, vacuum sealed, and double packed. Samples for X-ray radiography were taken separately as 20-cm-long thin slabs. The slab samples were taken continuously throughout cores using a plastic case of 20 × 2 × 0.7 cm in size and immediately sealed. These samples were sent to the University of Tokyo and stored in a refrigerator under 10°C. All the samples taken from Core 1H (197 samples) and every other sample from Core 2H (168 samples) were subject to inorganic geochemical analyses.

For X-ray diffraction (XRD), X-ray fluorescence (XRF), and carbon analyses, ~12 g of wet samples were washed and centrifuged twice with double distilled water to completely remove salts. The centrifuged samples were dried at 50°C for 24–48 hr, powdered with an agate mortar, and stored in glass tubes.

For grain-size analysis, the following three steps of chemical treatment, which are modified from the procedure of Rea and Janecek (1981), were applied to the samples to isolate the detrital component. Because the studied samples contain only trace amounts of siliceous bioclasts, an opal removal treatment was not conducted.

Step 1. Sea salt and Fe-Mn oxides removal. A dithionite-citrate system buffered with sodium bicarbonate was used (Mehra and Jackson, 1960). Approximately 0.06 g of sample was placed in a 70-cm³ centrifuge tube and 40 mL of 0.3-M sodium citrate and 5 mL of 1.0-M sodium bicarbonate were added. The tubes were placed in a 80°C water bath, ~1 g of sodium hydrosulfite was added, and it was stirred well. After 8 hr of

reaction, dispersed samples were centrifuged until the supernatant became clear and was then siphoned off. Samples were washed with 50 cm³ of 0.3-M sodium citrate and then with 50 cm³ of filtered deionized water (DIFW) and centrifuged.

Step 2. Carbonate removal. Forty cubic centimeters of 20 vol% acetic acid was added to samples and stirred. Dispersed samples were shaken for 8 hr. Then samples were centrifuged until the supernatant became clear and was then siphoned off. Samples were washed with 50 cm³ of DIFW and centrifuged.

Step 3. Organic removal. Approximately 40 mL of 10% H₂O₂ was added to samples, and the centrifuge tubes were placed in a 60°C water bath until the bubbling reaction stopped. The samples were then centrifuged until the supernatant became clear and was then siphoned off. Samples were washed with 50 cm³ of DIFW and centrifuged.

After this chemical leaching procedure, samples were kept wet to prevent aggregation. All the treated samples were introduced into the grain-size analyzer to prevent grain-size segregation during transfer.

ANALYTICAL METHODS

Organic and Carbonate Carbon Analysis

Total carbon and organic carbon contents were determined for all the samples studied using a LECO WR-12 carbon determinator. Approximately 0.1 g of powdered sample was weighed in a ceramic crucible and oxidized at 1500°C for 55 s, and the evolved CO₂ gas was measured to obtain total carbon content (tot-C). For determination of organic carbon content (org-C), approximately 0.1 g of powdered sample was treated with 2-N HCl for 24 hr and then dried at 60°C within a permeable crucible for 2 days. Carbonate carbon content (carb-C) was calculated by tot-C minus org-C. The precision of measurement was better than ±0.05 wt%.

Mineral Composition Analysis

Semiquantitative analysis of bulk mineral composition was conducted for all the samples using a MAC Science MXP-3 X-ray diffractometer equipped with CuK α tube and monochromator. Measurements were conducted at tube voltage of 40 kV and tube current of 20 mA with variable slit system that automatically controls a 25-mm beam width on the sample. Scanning speed was 4° 2 θ /min, and data sampling step was 0.02° 2 θ . A powdered sample was mounted on a glass holder and X-rayed from 2° to 40° 2 θ . Before reading out the positions and heights of diagnostic reflections, two steps of data processing were applied. As a first step, original data were smoothed by 5-pt. averaging, which is equivalent to a smoothing window width of 0.1° 2 θ . This process minimizes an error caused by noise. As a second step, a background-including amorphous hump was estimated by the background evaluation program, which uses a wider smoothing window with 30-pt. (equivalent to 6° 2 θ) between 10° and 40° 2 θ . Because the smectite peak is broad (~6° 2 θ in width), a smoothing window of 100-pt. (equivalent to 20° 2 θ) was used between 2° and 10° 2 θ . The background profile is subtracted from the 5-pt. smoothed profile to obtain the net peak intensities of crystalline minerals other than smectite. The background profile using a 100-pt. smoothing window was used for smectite.

Identification of minerals is based on the following diagnostic peaks; 7.2° for smectite, 8.8° for illite, 12.1° for chlorite + kaolinite, 26.6° for quartz, 27.8° for feldspars, 29.3° for calcite, and 32.9° for pyrite. Amorphous material, which includes poorly crystalline aluminosilicate, organic matter, and opal, is identified and semiquantified based on a broad hump between 16° and 32.5°. A reference sample was measured twice per day to correct for the drift of measurement condition. The peak intensities of the minerals were used to semi-

quantitatively determine mineral abundance. The reproducibility of the measurement is better than $\pm 7\%$ for quartz, $\pm 10\%$ for amorphous hump, $\pm 15\%$ for feldspars, $\pm 20\%$ for calcite, pyrite and smectite, and $\pm 30\%$ for illite and chlorite + kaolinite.

Major Element Composition Analysis

The concentrations of 10 major elements (SiO_2 , TiO_2 , Al_2O_3 , Fe_2O_3 , MnO , MgO , CaO , Na_2O , K_2O , and P_2O_5) were determined for all the samples by XRF analysis using a Rigaku 3270 spectrometer equipped with a Rh tube at the Ocean Research Institute, the University of Tokyo. The measurement was carried out on a fused glass bead at an acceleration voltage of 50 kV and a current of 50 mA. Powdered samples were dried at 110°C for more than 4 hr and then ignited at 1000°C for 6 hr to remove volatiles. Loss on ignition (LOI) was calculated from the weight loss. Approximately 0.4 g of ignited samples were mixed with ~ 4 g of $\text{Li}_2\text{B}_4\text{O}_7$ flux with the exact ratio of 1.000:10.00, and fused in a platinum crucible to make glass beads within 8 hr after ignition so as to avoid weight changes due to absorption of H_2O and CO_2 . A calibration curve was constructed using 40 standard samples provided from the Geological Survey of Japan, the United States Geological Survey, and the National Bureau of Standards (Irimo and Tada, 2000). The reproducibility (95% reliability) of measurement in relative scale is $\pm 0.6\%$ for SiO_2 , $\pm 0.8\%$ for TiO_2 , $\pm 0.7\%$ for Al_2O_3 , $\pm 0.7\%$ for Fe_2O_3 , $\pm 1.4\%$ for MnO , $\pm 1.0\%$ for MgO , $\pm 0.8\%$ for CaO , $\pm 1.6\%$ for Na_2O , $\pm 0.7\%$ for K_2O , and $\pm 1.2\%$ for P_2O_5 .

Grain-Size Analysis

We analyzed grain-size distribution of 79 selected samples by a laser diffraction-scattering method using Horiba LA-920 Grain Size Analyzer equipped with tungsten and He-Ne laser light sources. An entire pretreated sample was introduced into the analyzer with ~ 300 cm^3 of 0.2% sodium pyrophosphate solution, which aided dispersion of particles. Sample dispersion was circulated in a closed-tube system with in situ ultrasonification for 20 min before measurement. The result was transformed into volumetric grain-size distribution. Measurement was conducted from 0.02 to 2000 μm in diameter, with grain-size class of every $\Delta \log_{10}(\mu\text{m}) = 0.06$ (total 85 classes).

Because the analyzed samples occasionally showed tri- or bimodal grain-size distribution, we resolved the grain-size distribution curve into two or three log normal distribution curves using a repetitive numerical curve fitting by the IgorTM computer program. Relative error (1σ) of grain-size parameters for “fine” (~ 12 μm) and “coarse” (~ 57 μm) size fraction mode were $\pm 5\%$ for the mode position ($\log_{10}[\mu\text{m}]$), $\pm 13\%$ for the amount of mode, and $\pm 15\%$ for the mode width ($\log_{10}[\mu\text{m}]$). Those for “very fine” (~ 3 μm) mode were $\pm 5\%$ for the mode position ($\log_{10}[\mu\text{m}]$), $\pm 57\%$ for the amount of mode, and $\pm 16\%$ for the mode width ($\log_{10}[\mu\text{m}]$).

ANALYTICAL RESULTS

Organic and Carbonate Carbon Contents

Organic carbon content (org-C) of the studied samples varies between 0.30% and 3.00% with an average of 1.60 wt% (Appendix A). Org-C is relatively high and decreases downward from 3.00 wt% to 1.65 wt% with decimeter-scale low-amplitude ($<0.5\%$) fluctuations in the Holocene (Fig. 5). The decreasing trend is interrupted by a high org-C peak at 2.2 mbsf. Org-C is low between 1.0 wt% and 1.6 wt% within the Younger Dryas and high between 1.6 wt% and 2.3 wt% within the Bølling/Allerød. Org-C is low and shows centimeter- to decimeter-scale high-amplitude fluctuations between 0.30 wt% and 1.67 wt% in MIS 2 where low org-C peaks coincide with sand layers. In MIS 3 to 5a (5.2–15.1 mbsf), org-C shows decimeter-scale fluctuations with org-C maxima (1.4 wt%–2.0 wt%) generally occurring within silty clay with opaque filaments and/or particles and org-C

minima (0.7 wt%–1.4 wt%) generally occurring within clayey silt with occasional faint laminations. Within the lower part of this interval, org-C minima coincide with sand layers at 14.3, 14.45, and 14.75 mbsf.

Carbonate carbon content (carb-C) of the studied samples varies between 0.2 wt% and 2.0 wt% with an average of 0.81 wt%. Carb-C is relatively high (0.7 wt%–2.0 wt% with an average of 1.1 wt%) (Appendix A) in the Holocene, where it gradually increases downward from 0.8 wt% at core top to 2.0 wt% at 2.1 mbsf (Fig. 5). Carb-C suddenly drops to 0.6 wt% within the Younger Dryas and goes up again to 1.3 wt% within the Bølling/Allerød. Within MIS 2, carb-C varies in centimeter- to decimeter-scale between 1.2 wt% and 0.2 wt% with carb-C minima coinciding with sand layers. In MIS 3 to 5a, carb-C shows decimeter-scale fluctuations between 1.3 wt% and 0.3 wt%. Within this interval, carb-C minima below 0.4 wt% occur at 5.5, 8.2, 8.9, 11.5, 13.1, and 13.7 mbsf. No distinct sand layers are present within these intervals, but indistinct sandy zones and sharp contact surfaces are present. The intervals with carb-C maxima tend to coincide with silty clay and with opaque filaments and/or particles.

Mineral Composition

Quartz, feldspar, smectite, illite, chlorite + kaolinite, calcite, pyrite, and amorphous material are identified in all the samples (Appendix A), and we categorized these minerals into five groups based on the positive correlations of their peak heights and similarities in their vertical variation profiles (Fig. 6).

The first group is quartz and feldspar, which show a strong positive correlation ($r^2 = 0.64$). Vertical profiles of quartz and feldspar are generally similar (Fig. 6A). They are relatively low in the Holocene, significantly high in the Younger Dryas, and the lowest within the Bølling/Allerød. They are intermediate to high, with high-amplitude variations in MIS 2 with their maxima coinciding with sand layers. Within MIS 3, they are intermediate with decimeter-scale fluctuations with their maxima tending to coincide with faintly laminated and/or sandy intervals. Within MIS 4 to 5a, they are intermediate to high with decimeter-scale fluctuations. It is interesting to note that their minima tend to coincide with sand layers at 13.8, 14.3, 14.5, and 14.75 mbsf, which is opposite to what is observed in MIS 2.

The second group is illite, chlorite + kaolinite, and smectite. Among these clay minerals, illite has a strong positive correlation with chlorite + kaolinite ($r^2 = 0.64$), whereas smectite has weak positive correlations with illite and chlorite + kaolinite ($r^2 = 0.29$ and 0.33, respectively). Illite and chlorite + kaolinite have almost no correlation with quartz and feldspar, whereas smectite has a weak negative correlation with quartz ($r^2 = 0.28$). Within the Holocene, the three minerals gradually increase downward with small-amplitude, decimeter-scale fluctuations (Fig. 6B). Smectite decreases significantly within the Younger Dryas and increases to its maximum within the Bølling/Allerød, whereas illite and chlorite + kaolinite are not significantly changed within these intervals. Within MIS 2, the three minerals reach their maxima at 3.4 mbsf, then gradually decrease downward with large-amplitude fluctuations to 5.0 mbsf, with their minima coinciding with sand layers. Between 5.0 and 6.0 mbsf in the uppermost part of MIS 3, abundance of the three minerals are very low, then rapidly increases downward. Within MIS 3, they are intermediate to high with distinct maxima at 7.7, 8.3, 10.3, and 11.5 mbsf. Within MIS 4, they are relatively low, but gradually increase downward in MIS 5a. Within MIS 3 to MIS 5a, decimeter-scale, moderate- to large-amplitude fluctuations are present throughout with their minima, tending to coincide with the intervals of faint laminations and sandy zones.

The third group is calcite, which shows a weak positive correlation with amorphous material ($r^2 = 0.25$) and weak negative correlations with quartz and feldspar ($r^2 = 0.33$ and 0.32, respectively). Calcite has a strong positive correlation with carb-C ($r^2 = 0.75$), suggesting that calcite is the dominant phase of carbonate minerals.

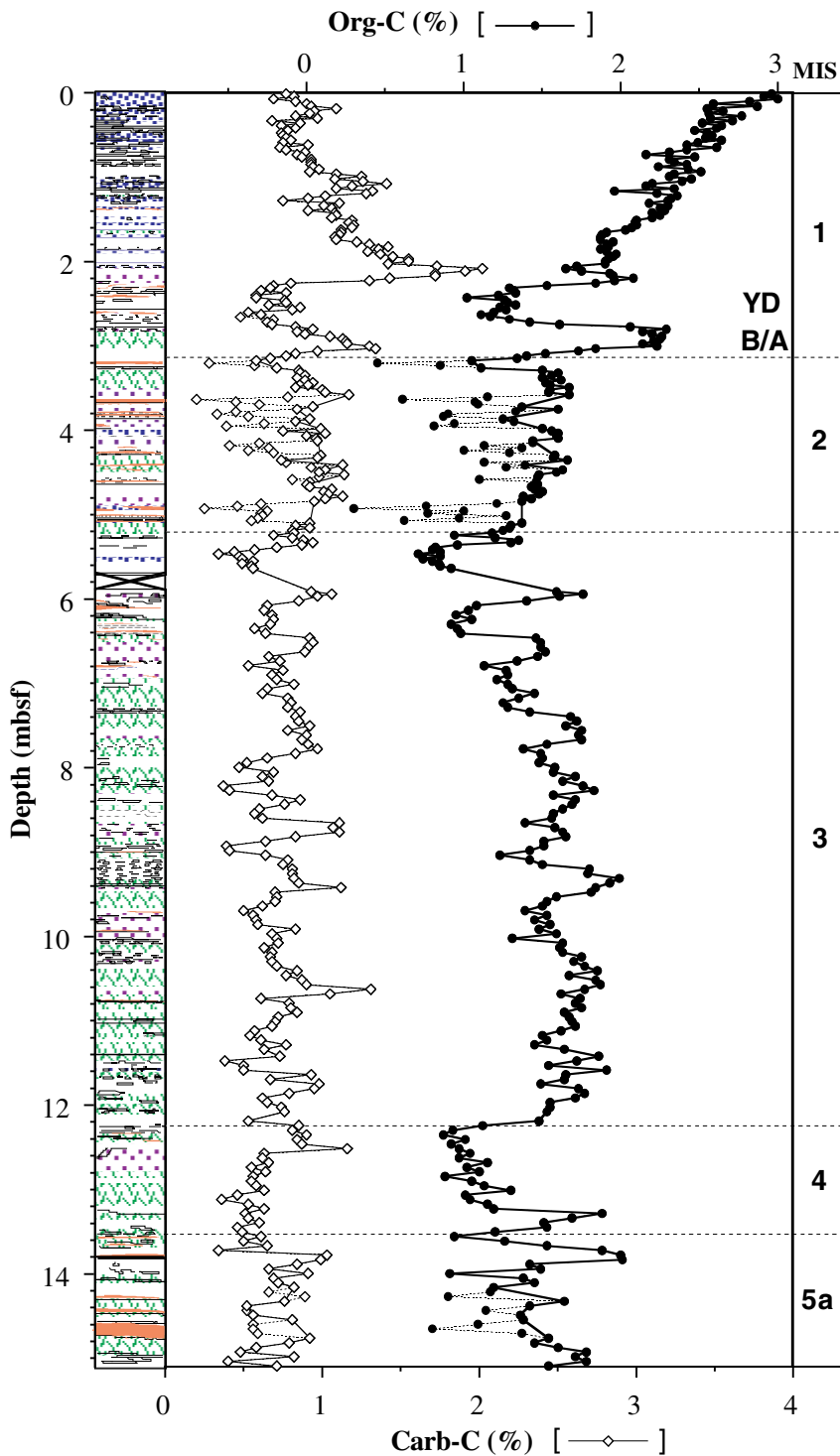


Figure 5. Vertical variations of org-C and carb-C in relation to lithology for the top 15 m of Hole 1017E. Turbidite sand samples are connected with thin dotted line. Lithology patterns defined in Figure 2.

Consequently, the vertical profile of calcite is basically similar to that of carb-C (Fig. 6C).

The fourth group is amorphous material. The area of amorphous hump has a weak positive correlation with calcite as described above and weak negative correlations with quartz and feldspar ($r^2 = 0.39$ and 0.36 , respectively). The area has a strong positive correlation with org-C ($r^2 = 0.69$). Consequently, its vertical profile is basically similar to that of org-C (Fig. 6C).

The fifth group is pyrite. Pyrite shows no correlation with other mineral phases. Pyrite is almost absent in surface sediments, but increases rapidly between 5 and 10 cmbsf (Fig. 6D). Within the Holocene, pyrite is intermediate to high with indistinct maxima at the middle of the interval. Pyrite is slightly low in the Younger Dryas and increases abruptly to form a distinct maximum in the Bølling/Allerød. It decreases abruptly at the top of MIS 2, gradually increases downward toward 4.2 mbsf, and gradually decreases again toward 5.5 mbsf at the top of MIS 3. Within MIS 2, moderate-amplitude centimeter- to decimeter-scale fluctuations are present with its minima occasionally coinciding with sand layers. Within MIS 3 to 5a, pyrite shows large-amplitude decimeter-scale fluctuations with its maxima coinciding with homogeneous silty clay with opaque filaments or disseminated particles. Distinct maxima of pyrite abundance are present

Consequently, the vertical profile of calcite is basically similar to that of carb-C (Fig. 6C).

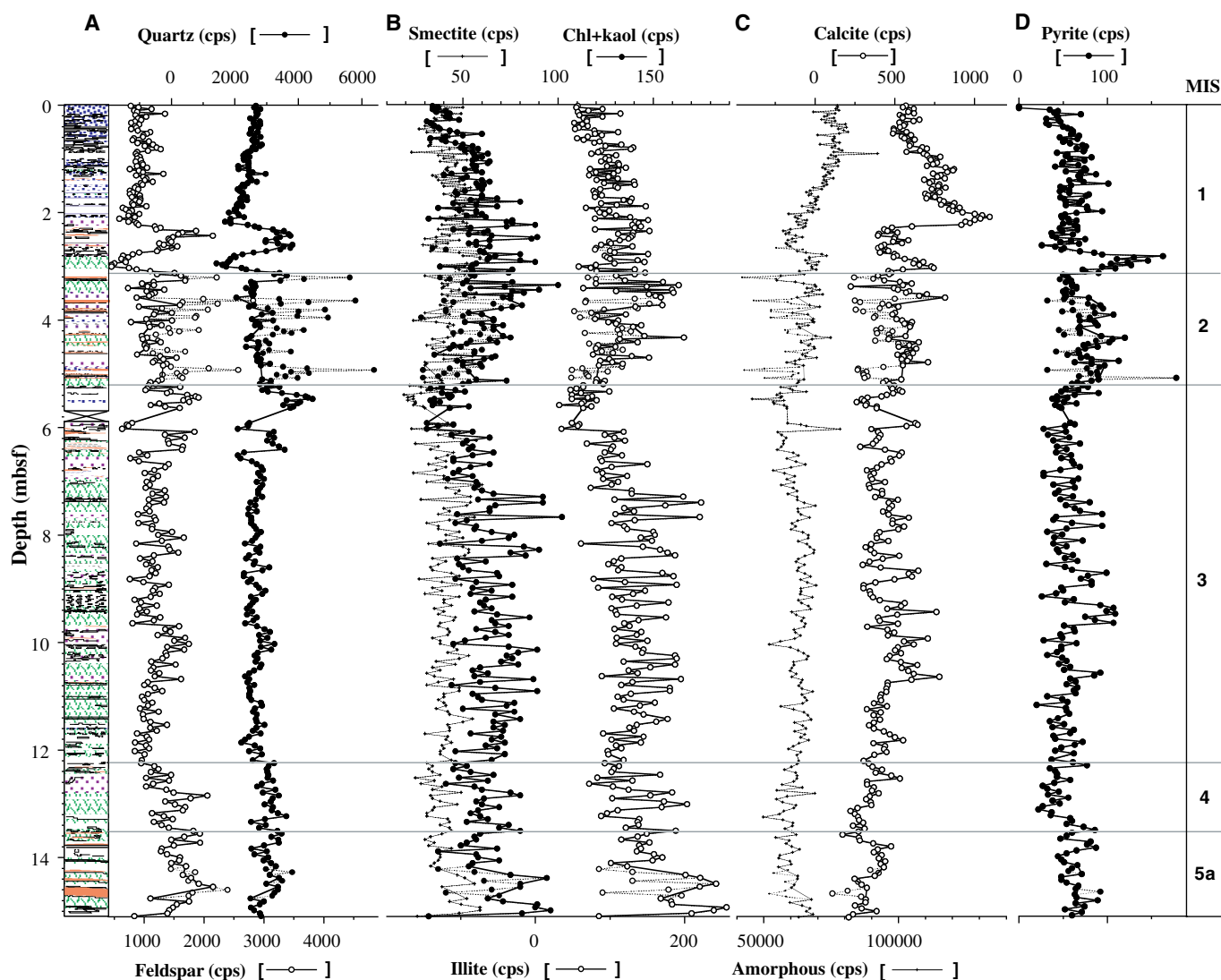


Figure 6. Vertical variations of peak heights of (A) quartz and feldspar; (B) smectite, illite, and chlorite + kaolinite; (C) calcite and amorphous material (peak area); and (D) pyrite for the top 15 m of Hole 1017E. Turbidite sand samples are connected with thin dotted lines. Lithology patterns defined in Figure 2.

at 7.7, 8.8, 9.5, and 10.6 mbsf in the middle of MIS 3, at 13.5 and 13.8 mbsf in the lower part of MIS 4, and at 14.8 mbsf in MIS 5a.

Major Element Composition

The ten major elements analyzed by XRF (including LOI; Appendix B) are categorized into five groups based on their interrelationships and similarities in their vertical variation profiles (Fig. 7). The first group (group 1) is SiO_2 , Na_2O , and K_2O , which show strong positive correlations with each other ($r^2 = 0.62\text{--}0.82$). These elements are generally low and gradually decrease downward to a minimum at 2.2 mbsf within the Holocene (Fig. 7A). An exception is Na_2O , which shows a small maximum at 1.8 mbsf. Group 1 elements increase drastically in the Younger Dryas, which then decrease drastically within the Bølling/Allerød. Within MIS 2, group 1 elements are intermediate to high and show high-amplitude fluctuations with their maxima coinciding with sand layers. Group 1 elements are high in the uppermost part of MIS 3, gradually decrease toward the middle part, and remain about the same in the lower part. They are relatively high within MIS 4 to 5a. Superimposed on this trend within MIS 3 to 5a is moderate-amplitude, decimeter-scale fluctuations with higher values tending to coincide with intervals with faint lamination and sandy zones. The maxima in MIS 5a correspond to sand layers.

The second group (group 2) is Fe_2O_3 and MgO , which have a strong positive correlation ($r^2 = 0.73$). Group 2 elements show moderate to strong negative correlations with SiO_2 ($r^2 = 0.52$ and 0.60 , respectively) and moderate to weak negative correlations with Na_2O and K_2O ($r^2 = 0.44$ to 0.24 , respectively). Vertical profiles of these elements are basically mirror images of those of SiO_2 (Fig. 7B). Exceptions are at 10.6, 11.4, and 14.65 mbsf, where either Fe_2O_3 or MgO varies in phase with SiO_2 .

The third group (group 3) is CaO and LOI, which show a strong positive correlation ($r^2 = 0.68$). CaO does not show positive correlations with any other elements, whereas LOI shows moderate positive correlations with Fe_2O_3 and MgO ($r^2 = 0.41$ and 0.50 , respectively). CaO and LOI show strong negative correlations with group 1 elements ($r^2 = 0.66\text{--}0.77$ and $0.65\text{--}0.92$, respectively). CaO also shows a strong correlation with carb-C ($r^2 = 0.82$), suggesting that this element is contained primarily in carbonate minerals, whereas LOI shows a strong correlation with org-C ($r^2 = 0.78$) and a moderate correlation with carb-C ($r^2 = 0.59$), suggesting that it dominantly represents organic matter and carbonate minerals. Calculation of weight loss due to ignition of carbonate mineral and organic matter by assuming CaCO_3 and CH_2O stoichiometry shows that ~80% of LOI can be explained by these two phases. Vertical profile of CaO and LOI is basically similar to that of carb-C and org-C, respectively (Fig. 7C).

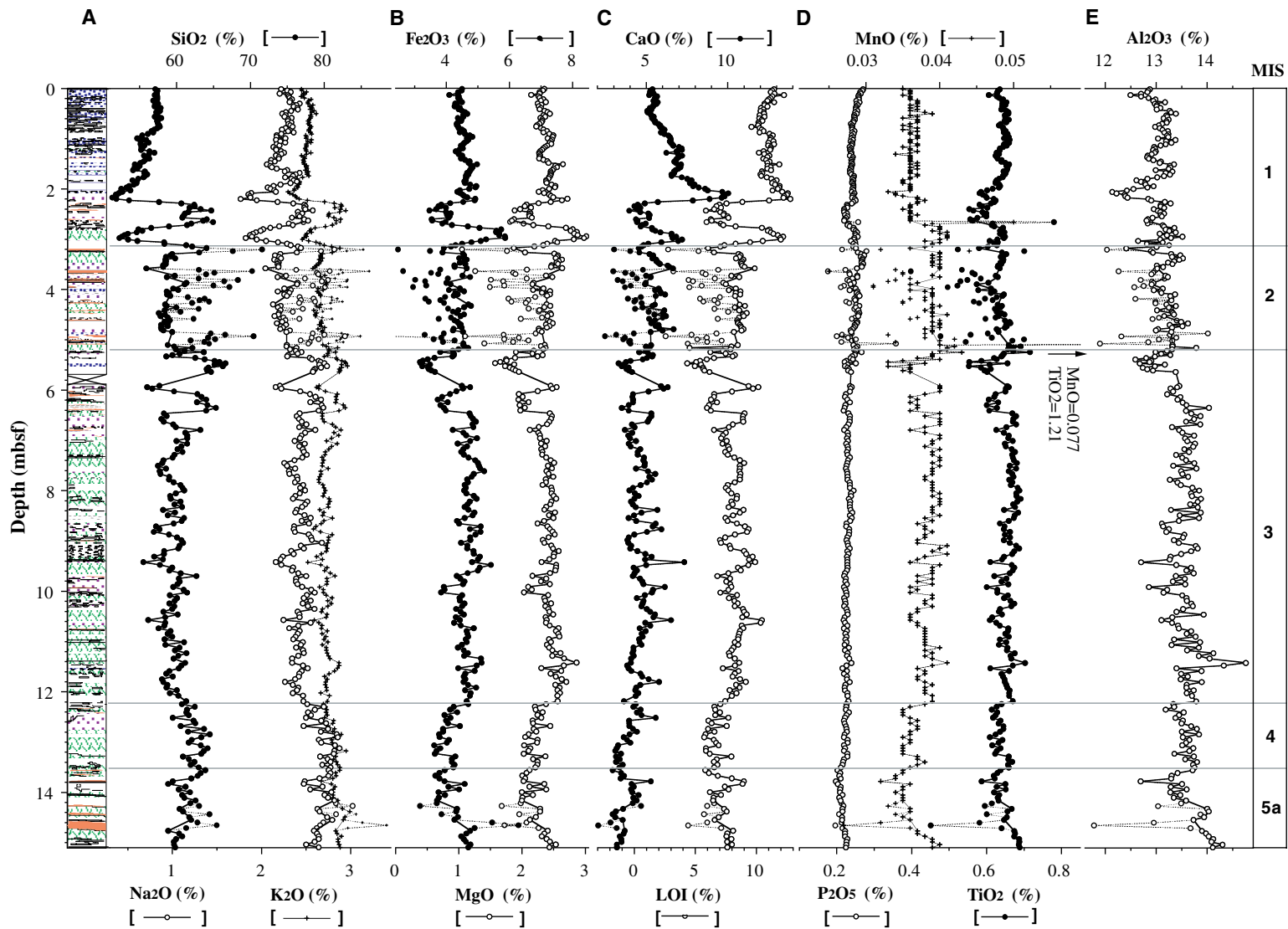


Figure 7. Vertical variations of element concentration of (A) SiO₂, Na₂O, and K₂O; (B) Fe₂O₃ and MgO; (C) CaO and LOI; (D) TiO₂, MnO, and P₂O₅; and (E) Al₂O₃ for the top 15 m of Hole 1017E. Turbidite sand samples are connected with thin dotted lines. Lithology patterns defined in Figure 2.

The fourth group (group 4) is TiO₂, MnO, and P₂O₅. TiO₂ and MnO show a strong positive correlation ($r^2 = 0.73$), whereas P₂O₅ shows only weak positive correlations with MnO and TiO₂ ($r^2 = 0.36$ and 0.21 , respectively). Group 4 elements do not show any correlation with other elements. Vertical profiles of TiO₂ and MnO are very similar, and P₂O₅ is also similar in many respects (Fig. 7D). Namely, these elements vary with only small amplitude with depth throughout the sequence except for several samples. Those samples showing the lower concentrations correspond to sand layers and sandy intervals, whereas those samples with the higher concentrations occur at the base of some sand layers and a sandy interval. Although vertical variations are small, there are slight variations with depth in the case of MnO and P₂O₅. MnO is slightly low within the Holocene to Younger Dryas and MIS 4 and slightly high within the Bølling/Allerød to MIS 3 and MIS 5a. In the case of P₂O₅, it is intermediate and slightly decreases downward in the Holocene to Younger Dryas, slightly high in the Bølling/Allerød to MIS 2, slightly low and gradually decreases downward in MIS 3 to MIS 4, and slightly increases in MIS 5a.

The fifth group (group 5) is Al₂O₃, which does not show correlations with any of other elements ($r^2 < 0.20$). Al₂O₃ does not vary significantly, but it is slightly low within the upper Holocene to MIS 2 (Fig. 7E). It increases abruptly at 5.6 mbsf in the uppermost part of MIS 3 and stays at that level downward throughout the rest of the sequence. Superimposed on this general trend are decimeter-scale fluctuations. Within the Holocene and MIS 3, most of Al₂O₃ minima correspond to carb-C maxima, suggesting that they reflect dilution by carbonate; the minima within MIS 2 and MIS 4 to 5a, however, correspond to sand layers, suggesting dilution by sand. In general, decimeter-scale fluctuations of Al₂O₃ are similar in phase with group 2 elements.

Factor Analysis of the Major Element Composition

Results of mineral and major element analyses suggest that variations in sediment composition can be explained by mixing of 4 or 5 end-member components. To make this point more clear, we applied Q-mode factor analysis to the data set of major element composition to identify and characterize common factors that control compositional variations. This method allows us to partition the sediment composition into the end-member components in the sediments.

Factor analysis provides a description of a multivariate data set in terms of fewer common factors that account for variance within the data set. Factor score and factor loading represent importance of each variable within each end-member and of each end-member within each sample, respectively. Factor scores and loadings generated by simple factor analysis are not scaled as (percent) fractions of variables within end-members and of end-members within samples, respectively. This fact prevents us from direct comparison of factor loadings with abundance of minerals, org-C, and carb-C. However, if the data are closed by constant total sum of variables in each sample, the factor scores and loadings can be converted into values expressed as (percent) fractions (Miesch, 1976). For this reason, we conducted Q-mode factor analysis for all the samples using concentrations of all the major elements including LOI (11 variables), of which total sum is constant at 100%. The largest number of variables and smallest analytical error for the major element composition data set allow us to examine the factors that explain only small fractions of variances in the data set.

Varimax rotation of factors was conducted to obtain geologically meaningful (preferentially positive) scores and loadings of components (Imbrie and van Andel, 1964). Analytical procedure is similar to Miesch (1976) and Leinen and Pisias (1984) except that we used all major elements and did not apply oblique rotation of the axes. Extracted factors are considered as representing end-member components (e.g., detrital, biogenic, and/or authigenic). Relative enrichment or depletion of elements between factors are expressed by factor scores, whereas relative contribution of factors between samples is

expressed by factor loadings. Because we did not apply oblique rotation of axes (Miesch, 1976; Leinen and Pisias, 1984), scores and loadings are only semiquantitative expressions of composition and content of factors, respectively.

Results of the analysis show that variance explained by each of the first five factors is significant (exceeding the range of analytical error) and they together explain 99.6% of the total variance. The first two factors alone explain nearly 95% of the variance, whereas factors 3 through 5 explain only 5% of the variance. However, concentration of certain elements in some of the samples can be explained only after inclusion of these factors in factor model. In other words, element concentrations not explained by factors 1 and 2 exceed analytical error of the elements. Therefore, we adopted a five-factor model to explain our data set. Extracted five factors are named as factor 1 through factor 5 in descending order of variance explained by each varimax factor. We also examined the meaning of extracted factors through correlation analysis between the factor loading and abundance of minerals, org-C, and carb-C of the samples. Composition scores of these elements for each factor are shown in Table 1, and correlation coefficients between org-C, carb-C, mineral composition, major element composition, and factor loadings are shown in Table 2.

Factor 1 explains 49.8% of variance and has larger (than average) scores for group 2 and 3 elements (Fe₂O₃, MgO, CaO, and LOI), and smaller (than average) scores for group 1 elements (SiO₂, Na₂O, K₂O). This factor shows strong to moderate positive correlations with org-C, carb-C, calcite, and amorphous material ($r^2 = 0.64 - 0.52$), a weak positive correlation with smectite ($r^2 = 0.24$), and strong negative correlations with quartz and feldspar ($r^2 = 0.81$ and 0.68 , respectively). Thus, this factor is characterized by higher contents of organic matter, carbonate, smectite, and amorphous material. Because the samples with larger loadings of this factor generally contain abundant nanofossils according to smear-slide observation, carbonate marking this factor is most likely of biogenic origin.

Factor 2 explains 45.1% of variance and has larger scores for group 1 elements and smaller scores for group 2 and 3 elements. This factor shows moderate positive correlations with quartz and feldspar ($r^2 = 0.53$ and 0.54 , respectively) and strong to moderate negative correlations with carb-C, org-C, calcite, and amorphous material ($r^2 = 0.82 - 0.43$). Thus, this factor represents a detrital component marked by quartz and feldspar.

Factor 3 explains 4.0% of variance and has larger scores for SiO₂, CaO, and LOI, and smaller scores for Al₂O₃, Fe₂O₃, MnO, and MgO. This factor shows faint positive correlations with quartz and calcite ($r^2 = 0.18$ and 0.12 , respectively) and weak to faint negative correlations with illite, chlorite + kaolinite, and smectite ($r^2 = 0.21 - 0.13$). Detailed examination of loading of this factor revealed that factor 3 tends to covary with factor 1 except for the intervals between 2.3 and 7.6 mbsf and 10.75 and 14.8 mbsf where frequent intercalations of sand layers and sandy zones occur (sandy intervals). This point is more clear on a scatter plot of factor 2 vs. factor 3 loadings in Figure 8A. In this figure, the two factors show a positive correlation for samples from the sandy intervals whereas the two factors show a negative correlation for samples from the intervals with hemipelagic silty clay to clayey silt without intercalations of sand layers (hemipelagic intervals). Within hemipelagic intervals, samples with higher factor 3 loadings tend to contain abundant planktonic foraminiferal skeletons (and nanofossils) according to smear-slide observation. On the other hand, within the sandy intervals, the samples with higher factor 3 loadings coincide with sand layers. Such samples contain abundant coarse-silt-size bioclasts that are composed of planktonic and benthic foraminiferal skeletons occasionally filled with pyrite and shell fragments. Thus, factor 3 seems to represent coarse-silt-size calcareous bioclasts of probable allochthonous origin within the sandy intervals and planktonic foraminifers of probable autochthonous origin within the hemipelagic intervals. The relation between factor 3 loading and quartz peak intensity in Figure 8B shows that samples from the sandy intervals show a positive correlation, whereas the samples from the

hemipelagic intervals show a negative correlation, which further supports this explanation.

Factor 4 explains 0.5% of variance and has larger scores for SiO_2 , TiO_2 , MnO , and P_2O_5 and smaller scores for Al_2O_3 , Fe_2O_3 , MgO , CaO , Na_2O , and LOI. This factor does not show correlation with any mineral phases and org-C. As is the case for group 4 elements, samples with extremely high factor 4 loadings occur at the base of sand layers and a sandy zone. However, it should be noted that not all sand layers have the basal part with high factor 4 loading—only the sand layers with very low org-C. It is possible that these high loadings reflect early diagenetic precipitation of MnO and P_2O_5 under early diagenetic oxic conditions that were temporarily caused by deposition of turbidite sand deficient in labile organic matter. But early diagenetic precipitation under temporal oxic environment cannot explain high concentration of TiO_2 . On the other hand, TiO_2 , MnO , and P_2O_5 in turbidite sand samples from MIS 2 show strong positive correlations each other ($r^2 > 0.82$) and a moderate to weak positive correlation with Fe_2O_3 ($r^2 > 0.37$), and stoichiometry estimated from these correlations is consistent with chemical composition of titanomagnetite. In addition, smear-slide observation suggests that the sample with highest factor 4 loading contains abundant heavy minerals including zircon, spinel, and magnetite. For these reasons, we prefer the interpretation that this factor represents condensation of heavy minerals probably including titanomagnetite that are condensed in the basal part of some of turbidite sand layers. The fact that factor 4 loadings are lower in other turbidite sands implies either different source(s) or sorting effect during transportation. Even after excluding these sand samples with exceptionally high or low factor 4 loadings, there still remains a variation in factor 4 loadings that is larger than analytical error. Namely, the loading is higher within MIS 2 and lower within MIS 5a. We suspect that this variation may reflect changes in composition of the detrital material. To test this possibility, we examined the relationship between factor 4 loading and $\text{Na}_2\text{O}/(\text{SiO}_2 - 14.15)$, a measure of deviation from the Na_2O vs. SiO_2 regression line, for the samples excluding turbidite sands (Fig. 9). The figure shows a clear negative correlation ($r^2 = 0.61$). Because both SiO_2 and Na_2O are considered as dominantly held in detrital material, this correlation strongly suggests that factor 4 represents a third detrital component.

Factor 5 explains 0.3% of variance and has larger scores for Fe_2O_3 , MgO , and K_2O and smaller scores for TiO_2 , MnO , and P_2O_5 . This factor shows a faint positive correlation with pyrite ($r^2 = 0.12$). Detailed examination of factor 5 loading revealed that samples with high factor 5 loading are restricted to three samples from a thick turbidite sand layer at 14.7 mbsf. This sand layer is characterized with abundant glauconite grains. Because glauconite is characterized with higher contents of Fe_2O_3 , MgO , and K_2O , it is likely that this factor represents glauconite. Smear-slide observation suggests that those samples with slightly high loadings of factor 5 also contain small amounts of glauconite grains.

Detrital Grain Size

Because grain-size distribution may reflect relative contribution of different transportation mechanisms and/or different detrital sources, we analyzed grain-size distribution of lithogenic fraction for selected samples, quantified relative amount of different size classes, and determined position of the principal mode. Seventy nine selected samples consist of 37 (every 6-cm interval) from the Holocene, two from the Bølling/Allerød, two from MIS 2, 37 (including 33 samples from every 6-cm interval) from MIS 3, and one from MIS 4. High-resolution sample sets were analyzed in two intervals to characterize decimeter-scale variations in sediment composition during the Holocene and MIS 3.

Grain-size distribution of these samples shows either unimodal or bimodal distribution with a shoulder on the finer side of the principal mode, and the distribution is resolved into two or three log normal grain-size distributions. The principal mode is located between 8 and 15 μm with average of 12 μm (termed “fine silt”) and the subordinate modes are located between 39 and 73 μm with an average of 57 μm (termed “coarse silt”) and between 2 and 4 μm with an average of 3 μm (termed “clay;” Fig. 10). The relative amount of each mode is different among samples and one of the subordinate modes is absent in several cases. Examples of the result of curve fitting are shown in Figure 10, and the relative amounts of each mode for analyzed samples are listed in Appendix C.

Fine silt is always a major fraction of the lithogenic component and its volume ranges from 59 to 86 vol%, whereas the volumes of coarse-silt and clay fractions range from 0 to 28 vol% and 5 to 27 vol%, respectively. The volumes of coarse- and fine-silt fractions have strong negative correlations ($r^2 = 0.74$), whereas volumes of clay, coarse-silt, and fine-silt fractions do not show a clear correlation between one another. This is partly due to the larger error associated with volume estimation of the fine-silt fraction.

Correlations between modal volumes and factor loadings are examined and results are listed in Table 3. It should be noted that the correlations are calculated for selected samples that do not include turbidite sands; consequently, they are heavily biased toward the Holocene and MIS 3. Factor 1 shows a faint positive correlation with fine silt ($r^2 = 0.17$) and a weak negative correlation with coarse-silt fraction ($r^2 = 0.29$), respectively. Factor 2 shows a faint positive correlation with coarse-silt fraction ($r^2 = 0.14$) and a faint negative correlation with fine-silt fraction ($r^2 = 0.10$). Factor 3 does not show any correlation with silt and clay fractions. Factor 4 shows a faint negative correlation with fine-silt fraction ($r^2 = 0.10$). Factor 5 shows a faint positive correlation with fine-silt fraction ($r^2 = 0.17$). It is also noteworthy that factor 5 shows moderate negative correlation with modal size of fine-silt fraction ($r^2 = 0.48$). The result suggests that factor 1 is preferably held in finer fractions (fine silt and clay), factors 2 and 4 in coarse-silt fraction, and factor 5 in fine-silt fraction. Factor 3 does not have special affinity to any size fractions. This is partly be-

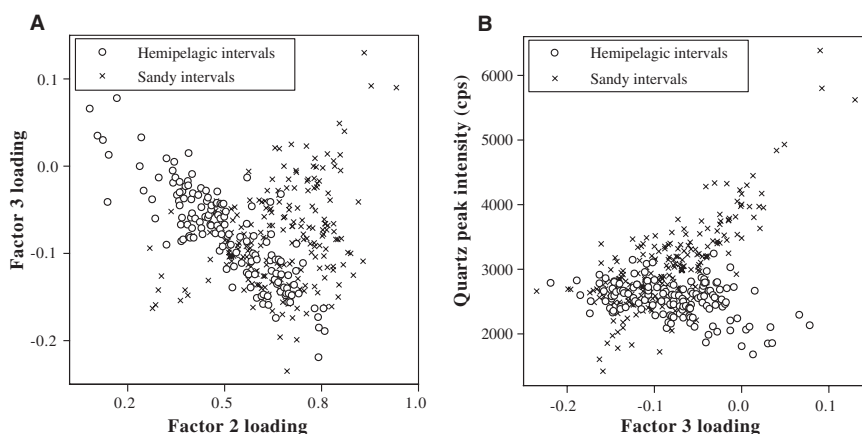


Figure 8. Diagrams showing the relationship between (A) factor 2 loading and factor 3 loading and (B) factor 3 loading and quartz peak height for samples from the top 15 m of Hole 1017E. In both diagrams, samples from sandy intervals (details in the text) show positive correlations whereas samples from hemipelagic intervals show negative correlations.

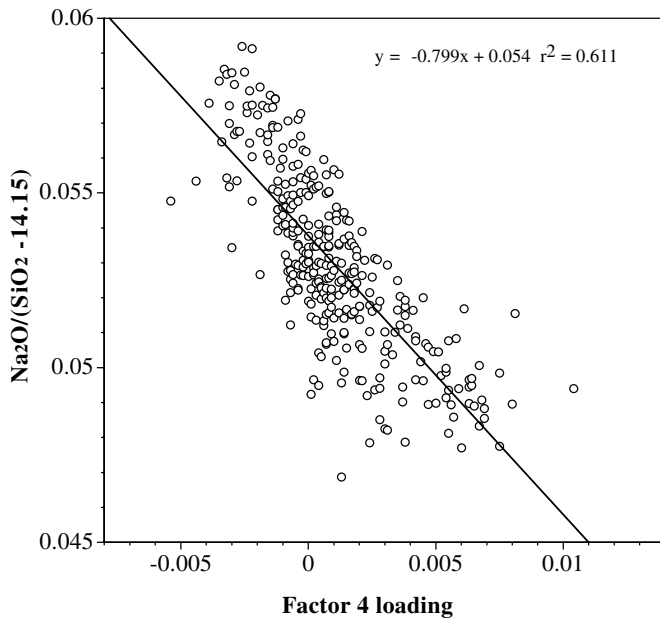


Figure 9. A diagram showing the relationship between factor 4 loading and $\text{Na}_2\text{O}/(\text{SiO}_2 - 14.15)$ for samples from the top 15 m of Hole 1017E. $\text{Na}_2\text{O}/(\text{SiO}_2 - 14.15)$ is a measure of deviation from the regression line of Na_2O and SiO_2 relation.

cause samples from sand layers, which commonly have higher factor 3 loadings, are not included and also because those grain-size parameters were determined for lithogenous fraction after acid treatment.

Vertical variations in volumes of each grain-size fraction and modal position of fine-silt fraction is shown in Figure 11. The volume of coarse-silt fraction is moderate and decreasing downward within the Holocene, low within the Bølling/Allerød, high during MIS 2, and moderate again in MIS 3. Variation of fine-silt fraction is basically a mirror image of the coarse-silt fraction, although a minimum corresponding to MIS 2 is not significant. The volume of clay fraction does not vary significantly except for one sample from the Bølling/Allerød where it is nearly twice as high. Superimposed on these trends are decimeter-scale variations that are obvious only within the intervals of high-resolution sample sets. Within the Holocene, the fine fraction shows three maxima at 0.95, 1.6, and 2.2 mbsf, whereas maxima are found at 7.6, 8.2, 8.4, and 8.8 mbsf within the middle of MIS 3. These maxima correlate well with the minima of factor 2 (and maxima of factor 1).

We also examined modal grain size of fine-silt fraction, which is clearly recognized on grain-size distribution diagram. Modal grain size of fine-silt fraction is relatively large (10.6–14.9 μm) in the Holocene. It abruptly decreases to 9.0 μm near the bottom of Holocene and then is small (8.0–8.7 μm) in the Bølling/Allerød, moderate around 10.5 μm in MIS 2, and moderate to large (10.0–13.5 μm) in MIS 3 (Fig. 11). Within the high resolution part of MIS 3, modal grain size shows maxima at 7.3, 7.8, 8.2, 8.5, and 8.8 mbsf that tend to coincide with the maxima of factor 2. Modal grain size of fine-silt fraction has a weak positive correlation ($r^2 = 0.27$) with the volume of coarse-silt fraction.

Degree of Pyritization

The degree of pyritization (DOP_T) used here is defined as the ratio of pyrite Fe within total Fe. It is commonly used to estimate relative (not absolute) levels of bottom-water oxygenation conditions with higher DOP_T suggesting less oxic conditions (Bernier, 1970, 1984; Calvert and Karlin, 1991; Tada et al., 1992). We estimated pyrite content from pyrite peak height on X-ray diffractograms using the

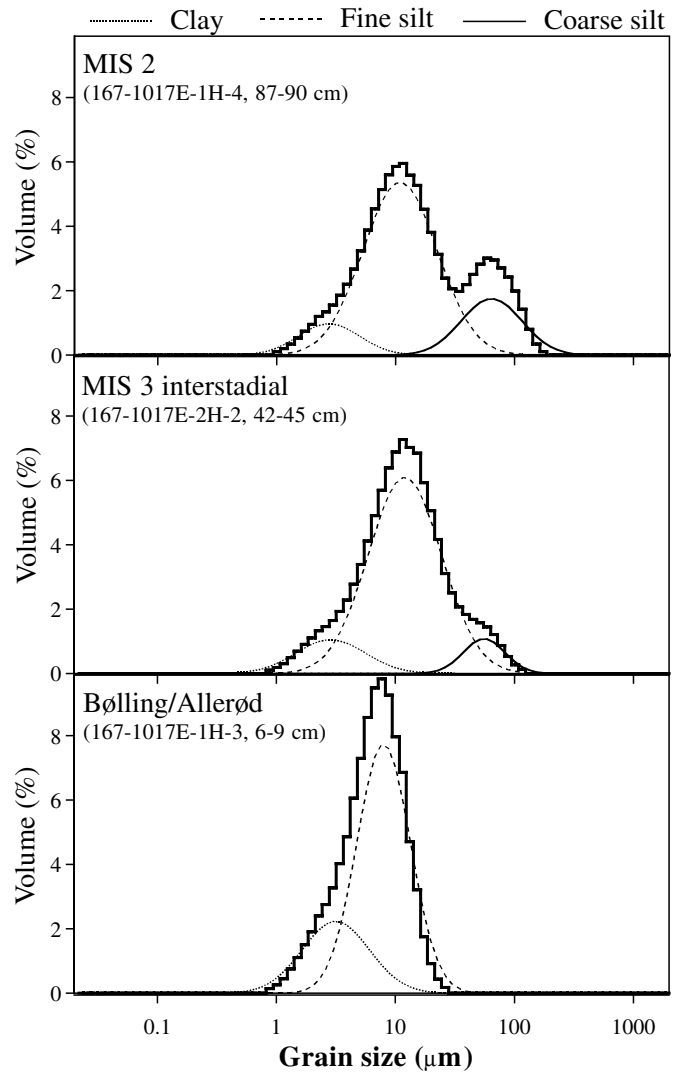


Figure 10. Three typical examples of grain-size distribution of lithogenous fraction for samples from the top 15 m of Hole 1017E. Result of curve fitting is also shown.

gression equation derived by Tada et al. (1999) to calculate DOP_T . DOP_T does not show any correlation with Fe_2O_3 nor loadings of any factors, suggesting that it is not strongly controlled by sediment composition. On the other hand, DOP_T shows a strong positive correlation with the pyrite-S/org-C ratio ($r^2 = 0.60$), which is another indicator of bottom water oxygenation level (Bernier and Raiswell, 1983), supporting the appropriateness to use DOP_T as a relative measure of the bottom-water oxygenation level. An org-C vs. pyrite-S plot (not shown) indicates that most of the samples analyzed fall within the range of normal marine of Bernier and Raiswell (1983) when samples from turbidite sands and the top 40 cmbsf were excluded. This implies that the bottom-water oxygenation level at the studied site did not become euxinic during the last 80 k.y. Excluding samples from the top 40 cmbsf, where active pyrite formation process seems still in progress, DOP_T of the studied samples varied between 0.06 and 0.32, with an average of 0.16.

Vertical profile of DOP_T is shown in Figure 12. DOP_T is high within the Bølling/Allerød and middle to lower part of MIS 2, intermediate within the Holocene and Younger Dryas, intermediate to high in MIS 5a, intermediate in the upper part of MIS 2, intermediate to low in MIS 3, and low in MIS 4. Superimposed on these trends are decimeter-scale fluctuations, which are most evident within MIS 3

Table 3. Correlation coefficients (r) between modal volumes, modal position of fine-silt fraction, and factor loadings.

	Fine silt position	Clay volume	Fine silt volume	Coarse silt volume	Factor 1	Factor 2	Factor 3	Factor 4	Factor 5
Fine silt position:	1.00								
Clay volume:	-0.21	1.00							
Fine silt volume:	-0.44	-0.14	1.00						
Coarse silt volume:	0.52	-0.39	-0.86	1.00					
Factor 1:	-0.32	0.30	0.41	-0.54	1.00				
Factor 2:	0.20	-0.16	-0.31	0.37	-0.91	1.00			
Factor 3:	0.17	-0.13	0.00	0.07	-0.21	-0.19	1.00		
Factor 4:	-0.15	0.12	-0.31	0.23	-0.03	-0.07	0.16	1.00	
Factor 5:	-0.69	0.08	0.41	-0.42	-0.03	-0.08	0.05	0.17	1.00

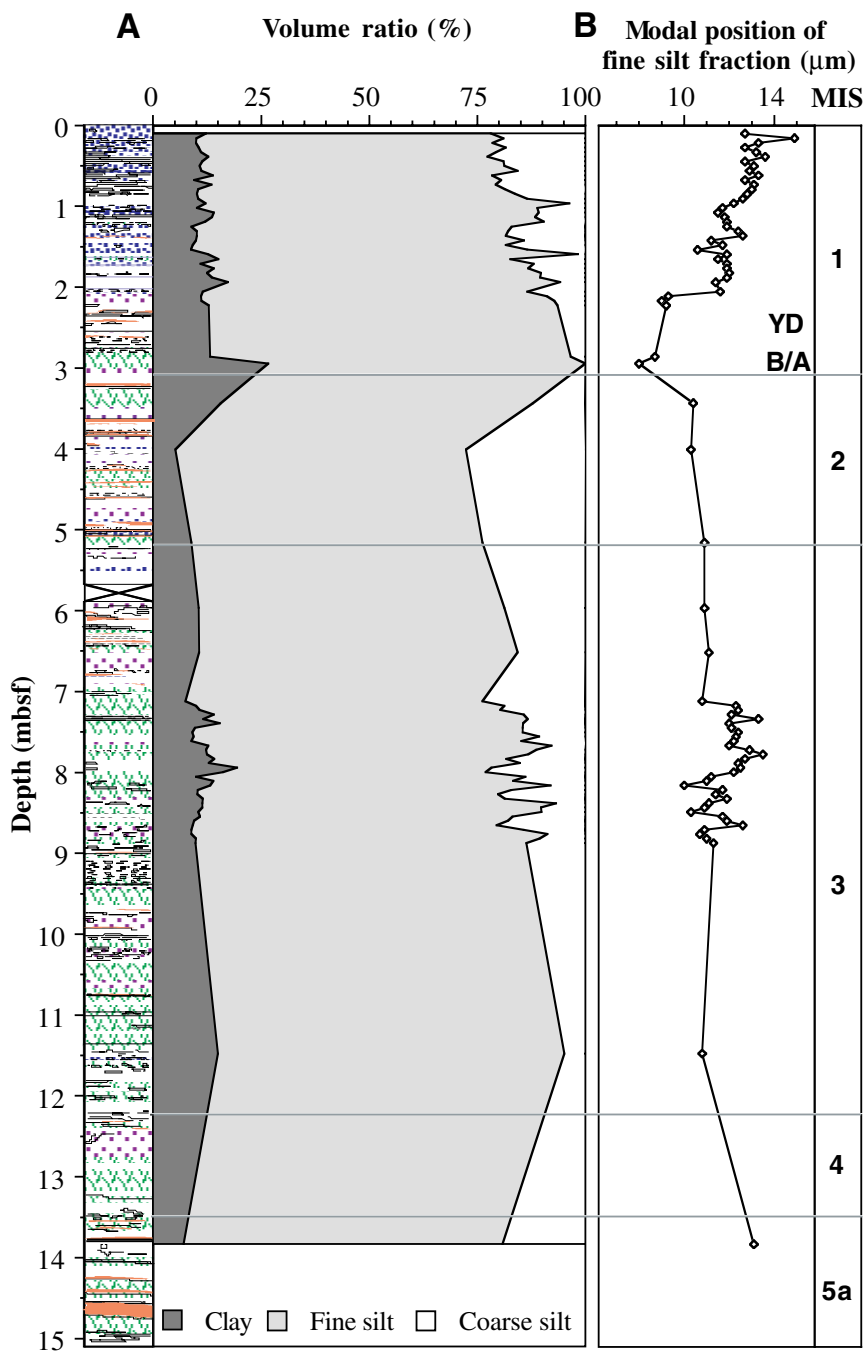


Figure 11. Vertical variations of (A) volume ratio of the three grain-size fractions and (B) modal position of fine-silt fraction for selected samples from the top 15 m of Hole 1017E. Lithology patterns defined in Figure 2.

where distinct DOP_T maxima occur approximately at 7.8, 8.8, 9.5, and 10.6 mbsf.

DISCUSSION

Compositional Variations and Their Paleooceanographic Implications

Temporal variations of loadings of factors 1 through 5, which basically explains temporal variation of sediment composition, are reconstructed based on the age model (Fig. 13; original data are listed in Appendix D). In Figure 13, the planktonic $\delta^{18}O$ profile of Kennett et al. (Chap. 21, this volume) is also shown (Fig. 13D) to examine variation of the sediment composition in relation to glacial/interglacial and stadial/interstadial changes.

Factors 1 and 2 (Grain-Size Indicator)

It is obvious from Figure 13 that loading of factor 1 is higher during the Holocene and Bølling/Allerød; intermediate during MIS 2, 3, and 5a; and lower during the Younger Dryas, uppermost part of MIS 3 (between 25 and 26 ka), and MIS 4 (Fig. 13A). During MIS 3, factor 1 loading is higher during interstadials and lower during stadials. Profile of factor 2 loading is almost a mirror image of factor 1 profile. These profiles also resemble the profile of planktonic $\delta^{18}O$. Because loadings of factors 1 and 2 semiquantitatively represent contribution from finer and coarser fraction of lithogenic component, these results suggest a strong linkage between climatic changes and variations in grain size of hemipelagic sediments with finer grain sizes during warmer periods and coarser sizes during cooler periods.

Observation of sedimentary structures shows that faint laminations and sharp contact surfaces occur within stadial intervals including the Younger Dryas. Parallel lamination could represent either varves formed by seasonal variations of surface productivity transmitted to the bottom sediments and preserved under anoxic bottom-water conditions or contourites formed by fluctuations of contour current velocity. Because varve-type laminations are found under anoxic conditions (e.g., Savrda et al., 1984), whereas contourites tend to be formed by highly ventilated intermediate- and deep-water flows, it is possible to distinguish the two types of lamination with evidence for anoxic conditions. We examined the relationship between DOP_T and the occurrence of faint laminations and sharp contact surfaces (Fig. 12) in which positions of faint laminations and sharp contact surfaces are indicated as arrows. As is obvious from Figure 12, faint laminations and sharp contact surfaces tend to coincide with intervals of lower DOP_T , suggesting more oxygenated bottom-water conditions during these intervals. This evidence argues for contourite origin of laminations and against varve origin. Lower contents of org-C and carb-C within these intervals are also against varve origin.

Contourites are characterized by well-sorted grain-size distributions with their mode in the medium- to coarse-silt size range (16–62 μm). In their study of contourites in the southern Weddell Sea, Weber et al. (1994) described laminated contourite whose principal mode is between 13 and 39 μm . On the other hand, our faintly laminated clayey silt samples are also well sorted and have the principal modal position at 13–14 μm . The agreement in the principal modal position together with the presence of faint parallel lamination suggests that our faintly laminated intervals (and also sharp contact surfaces) could be contourites. If this interpretation is correct, then compositional changes of the sediments explained by factors 1 and 2 should represent variations in grain size caused by changes in contour current intensities that were stronger during the Younger Dryas and stadials within MIS 3 and 4. Although grain-size analysis has not been conducted yet for samples from the Younger Dryas, low factor 1 loading within this interval suggests stronger contour current. Stronger con-

tour current during the Younger Dryas is consistent with low sedimentation rate at the basal part of this interval (Fig. 2).

Kennett and Ingram (1995) and Behl and Kennett (1996) suggested the possibility of increased ventilation of NPIW during the Younger Dryas and stadials during MIS 2 and 3 based on the ventilation history of the Santa Barbara Basin. Stronger contour current intensities with higher bottom-water oxygenation levels during stadials (including the Younger Dryas) and weaker current intensities with lower bottom-water oxygenation levels during interstadials (including the Bølling/Allerød) reconstructed here are consistent with their hypothesis. Together with their results, our result strongly argues for intensification of intermediate-water circulation in the North Pacific during stadials possibly associated with Dansgaard-Oeschger cycles in the last glacial episode.

Factor 3 (Possible Carbonate Dissolution Indicator)

When turbidite sand samples are excluded, factor 3 in hemipelagic sediments (including contourites) basically explains excess or deficiency of biogenic carbonate that are not explained by factor 1. It can be either representing carbonate productivity or dissolution. We do not have conclusive evidence to specify either of the two possibilities. However, when comparing the vertical profile of factor 3 with that of org-C, maxima of factor 3 coincide with minima of org-C in most cases (Fig. 13B). Because factors 1 and 3 are positively correlated when turbidite sand samples are excluded, this antiphase relation is not due to grain-size effect. A more plausible explanation is the dissolution of biogenic carbonate in samples rich in labile organic matter. A prominent maximum of carb-C at 10 ka is widely recognized in the sediments all over the world including the California margin and considered as reflecting better preservation of CaCO_3 (Broecker et al., 1993; Gardner et al., 1997). This interpretation is consistent with presence of prominent positive loading of factor 3 at 10 ka in the studied samples. Thus, we speculate that factor 3 may represent carbonate preservation, although we do not exclude the possibility of productivity contribution.

According to this interpretation, high carbonate preservation (or high production) occurred at 9.5, 16, 25, 46.5, and 75 ka. These high carbonate preservation (or production) events seem to coincide with those observed at Hole 1016C, ~100 km to the west of this site with water depth of 3835 m, by Yamamoto et al. (Chap. 12, this volume). However, poor age control at Site 1016 prevents us from detailed correlation. Carbonate preservation was relatively good (or production are relatively high) during the Holocene, MIS 2, and MIS 4, and low during the Bølling/Allerød, MIS 3, and MIS 5a. Higher carbonate preservation (or production) during MIS 2 is consistent with Lyle et al. (1992) who reported enhanced carbonate burial at 18 ka in a northern California margin transect.

Factor 4 (Provenance Indicator)

Factor 4 is considered as representing a third detrital component that dominantly explains variations of TiO_2 , MnO , and P_2O_5 and to some extent Fe_2O_3 , and probably represent titanomagnetite-like mineral. Significant variations in factor 4 loading are restricted to turbidite sand samples from MIS 2 that have either higher or lower loading compared to hemipelagic clayey silt and silty clay samples. We interpret this as reflecting sorting effect during transportation as described before. On the other hand, factor 4 loading of turbidite sand samples from MIS 5a does not show any deviation from adjacent hemipelagic sediments. This suggests either that turbidite has at least two different source areas or that sand composition of the source area changed with time. After excluding turbidite sand samples, factor 4 loading still shows some variations with higher loading during MIS 2 and lower loading during MIS 5a, middle of MIS 3 (approximately at 50 ka), and early part of the Holocene (Fig. 13C). Because titanomagnetite

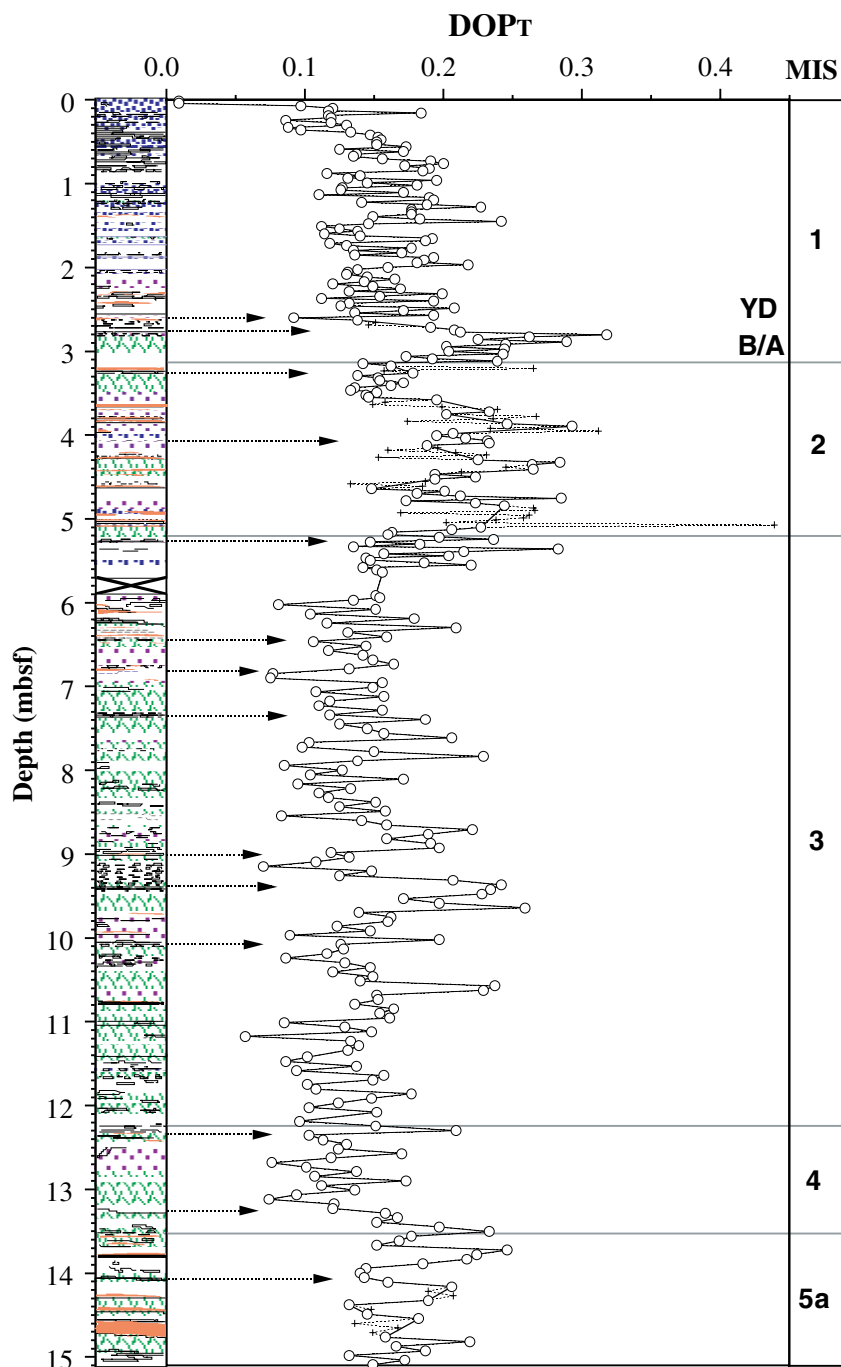


Figure 12. Vertical variations of DOP_T for the top 15 m of Hole 1017E. Turbidite sand samples are connected with thin dotted lines. Lithology patterns defined in Figure 2.

preferentially occurs in mafic and ultramafic rocks, and ultramafic rocks are mostly exposed along the coast to the north of Point Conception but not to the southeast of it, it is possible that this factor could represent a northern component of the detrital material transported along the coast. Further investigation is necessary to test this possibility.

Factor 5 (Glauconite Indicator)

Factor 5 explains some of the variations in Fe_2O_3 and K_2O and is considered as representing a glauconite component. When samples from a turbidite layer at 14.7 mbsf are excluded, loading of factor 5 is not large, but its variation is still larger than the noise. Temporal variations of factor 5 loading in Figure 13C shows that it is higher

during the Bølling/Allerød, and to a lesser extent the Younger Dryas and interstadials during MIS 3. Because the sediments deposited during these periods are characterized by hemipelagic clayey silt to silty clay without any interruption by turbidite, and hemipelagic samples with higher factor 5 loading do not agree with contourites, it is likely that glauconite in these sediments were formed in situ rather than re-worked.

Glauconite formation is favored by a marginally oxic environment (Odin and Matter, 1981), and high concentration of glauconite grains in the surface sediments are reported from the upper edge of OMZ approximately at 500 m water depth of central California margin (Mullins et al., 1985). Mullins et al. (1985) also reported high concentration of fecal pellets at the lower edge of OMZ at ~1000 m water depth. Because fecal pellets are a good substrate for glauconite-

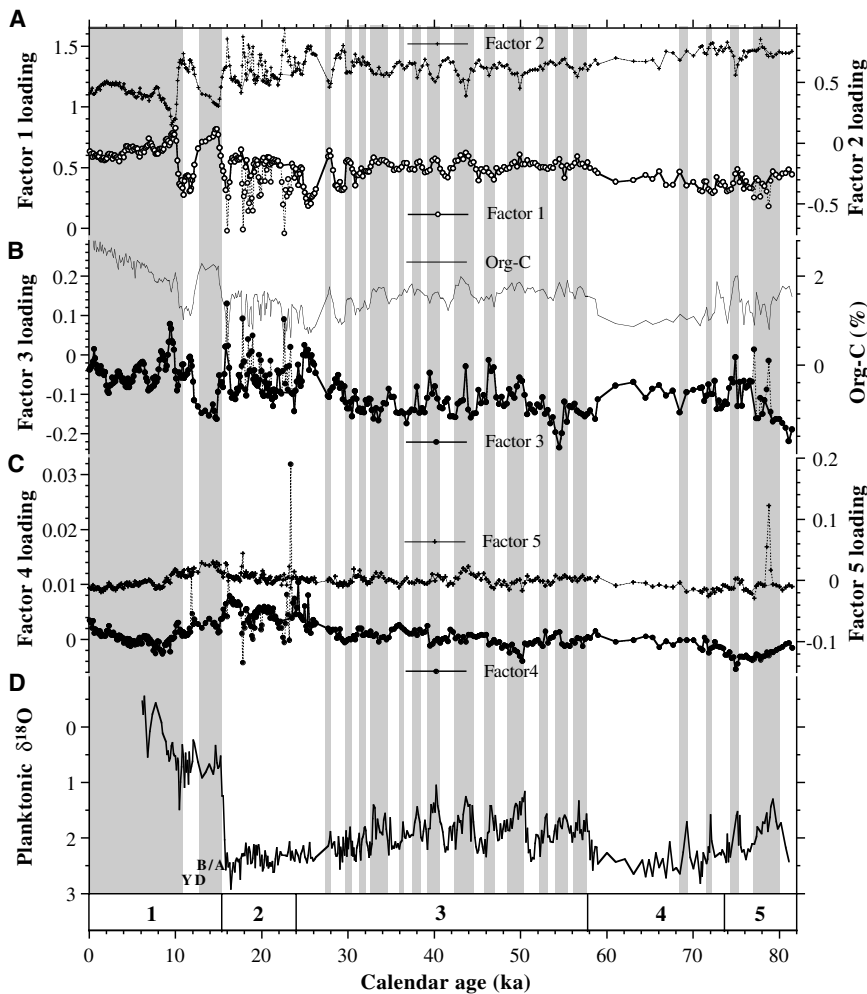


Figure 13. Temporal variations of loadings of (A) factors 1 and 2, (B) factor 3 and org-C, and (C) factors 4 and 5, in relation to (D) glacial/interglacial and stadial/interstadial climatic changes indicated by planktonic $\delta^{18}\text{O}$ variations. Turbidite sand samples are connected with thin dotted lines.

zation, it is possible that fecal pellets were glauconitized to some degree at the lower edge of OMZ. If this is the case, factor 5 might reflect behavior of OMZ with higher factor 5 loading corresponding to downward shift of the lower edge of OMZ.

Possible Factors Controlling Org-C Variations

Org-C is frequently used as an indicator of surface productivity although limitations of its usage are frequently discussed (e.g., Lyle et al., 1992). For the hemipelagic sediments analyzed in this study, org-C variations (which is included in LOI variations) are dominantly explained by factor 1, which represents finer fraction of the sediments. Through their study of surficial sediments from Washington margin, Keil et al. (1994) showed that >90% of the total organic carbon is sorbed on the inorganic mineral surfaces, and its concentration is strongly controlled by sediment surface area. Because sediment surface area increases with decreasing grain size, negative correlation between org-C and grain size is expected. This explains the clear positive correlation between factor 1 loading and org-C as shown in Figure 14. Similar relationship between org-C and grain size is also reported from laminated contourites from the southern Weddell Sea (Weber et al., 1994). Thus, org-C in the studied sediments is considered as principally controlled by grain size of lithogenic fraction that in turn reflects intensity of contour current.

Scattering from the regression line in Figure 14 may represent additional factor(s) that control org-C. Those samples that scatter to the larger org-C side of the regression line come from six intervals. These are the late Holocene (<1.5 mbsf), later part of the Younger Dryas (2.2–2.6 mbsf), three interstadials in the early half of MIS 3 (9.2–9.4,

10.0–10.5, and 11.4–11.6 mbsf), and MIS 5a (13.2–15.1 mbsf) (Fig. 14). Org-C higher than the regression line for the Holocene samples could be explained by temporal retention of metabolizable organic matter that will be decomposed during the course of early diagenesis within the top few meters (Gardner and Dartnell, 1995). Alternatively, it could be explained by enhanced preservation of organic carbon under poorly oxygenated bottom-water conditions (e.g., DeMaison and Moore, 1980; Canfield, 1994) implied from the presence of *Chondrites*-like burrows within the top 1.5 m. Higher org-C trends for other five intervals do not seem to be explained by either of these two factors. First, effect of temporal retention of metabolizable organic matter is unlikely because the continuous downward decreasing trend of org-C ceased at 2.3 mbsf, below which no downward decreasing trend is observable on org-C profile. Second, DOP_T values within these intervals are not necessarily high, although high DOP_T values occur in a few samples. Consequently, enhanced preservation under poorly oxygenated conditions does not seem important. A more plausible explanation is increased contribution of organic matter that is not associated with fine lithogenic particles. Increases in contribution of free organic matter to the sediments could be caused either by enhanced surface productivity or by enhanced supply of terrigenous organic matter, mostly through rivers. At this stage, we do not have enough data to specify the source of organic matter within these specific intervals, but increased supply of terrigenous organic matter is a possible explanation because three of these intervals coincide with the intervals with abundant plant fragments (Fig. 2). It is interesting to note that relative enrichment of org-C is not obvious for samples from the earliest Holocene or the Bølling/Allerød where high org-C and carb-C peaks are recognized.

SUMMARY

High-resolution analyses of mineral and major element composition including org-C and carb-C were conducted for the latest Pleistocene to Holocene sediments from ODP Site 1017 covering the last 80 k.y. Compositional variations associated with glacial/interglacial as well as millennial-scale changes in paleoceanographic conditions are identified at the intermediate depth of the California margin off Point Conception. Significant variations in mineral and major element composition were detected in both time scales, which were semiquantified subjectively by Q-mode factor analysis of 11 major elements. Five factors were extracted, which together explain more than 99% of variance. To characterize these five factors, correlation was examined between the factors and mineral composition. We also conducted grain-size analysis of selected samples to characterize grain size of these factors.

Factor 1 has high scores of Fe_2O_3 , MgO, CaO, and LOI and represents enrichment of fine-silt- to clay-size amorphous material (including organic matter), calcite, and smectite. Factor 2 has high scores of SiO_2 , Na_2O , and K_2O and represents enrichment of coarse-silt- (and sand) size quartz and feldspar. Factor 3 has high scores of SiO_2 , CaO, and P_2O_5 and represents enrichment of coarse-silt- to sand-size bioclasts and quartz in the case of turbidite sand, and fine-silt- to clay-size autochthonous biogenic carbonate in the case of hemipelagic sediments. It is likely that factor 3 in hemipelagic sediments represents the degree of carbonate preservation and/or productivity. Factor 4 has high scores of TiO_2 , MnO, and P_2O_5 and possibly represents enrichment of titanomagnetite-like mineral. This factor may represent a size-sorting effect during transportation in the case of turbidite sands and a possible northern source of detrital material in the case of hemipelagic sediments. Factor 5 has high scores of Fe_2O_3 , MgO, and K_2O and probably represents enrichment of glauconite. It is likely that glauconite in hemipelagic sediments is authigenic and could be related to the bottom-edge position of OMZ.

Grain-size distribution of hemipelagic sediments is well expressed by factors 1 and 2, which explains most of their compositional variations. Temporal variations of factor 1 (representing fine silt and clay) show millennial-scale as well as orbital-scale variations with higher loading (finer grain size) during warm periods and lower loading (coarser grain size) during cold periods. The intervals characterized by lower factor 1 loading coincide with faintly laminated intervals. Together with their principal grain sizes of 13–14 μm , these faintly laminated intervals are considered as contourites. These results suggest that bottom-current intensity at Site 1017 (water depth of 956 m) changes in concert with stadial/interstadial as well as glacial/interglacial climatic cycles during the last 80 k.y. with periods of stronger current intensities coinciding with cooler periods and vice versa. Relative bottom-water oxygen level inferred from DOP_T suggests that bottom water was better ventilated during cold periods when contour current intensity was stronger. This evidence argues for the hypothesis by Kennett and Ingram (1995) and Behl and Kennett (1996), which suggested the possibility of increased ventilation of NPIW during the Younger Dryas and stadials during the last glacial period. This, in turn, suggests intensification of intermediate-water circulation in the North Pacific during stadials of the last glacial episode, possibly associated with Dansgaard-Oeschger cycles.

Our result also suggests that org-C and carb-C, which are occasionally used as indicators of surface productivity, are strongly influenced by grain-size sorting caused by contour current at least at Site 1017 and possibly at other sites in the California margin. Only after subtracting the influence of grain-size effect do signals of productivity, preservation, or input from terrestrial source become evident. Correlation between org-C and factor 1 (fine-grain-size indicator) suggests presence of additional organic carbon at several stratigraphic intervals. These are tentatively attributed to metabolizable organic matter still contained within the top 1.4 m of the sequence and an additional supply of terrestrial organic carbon from nearby rivers and/

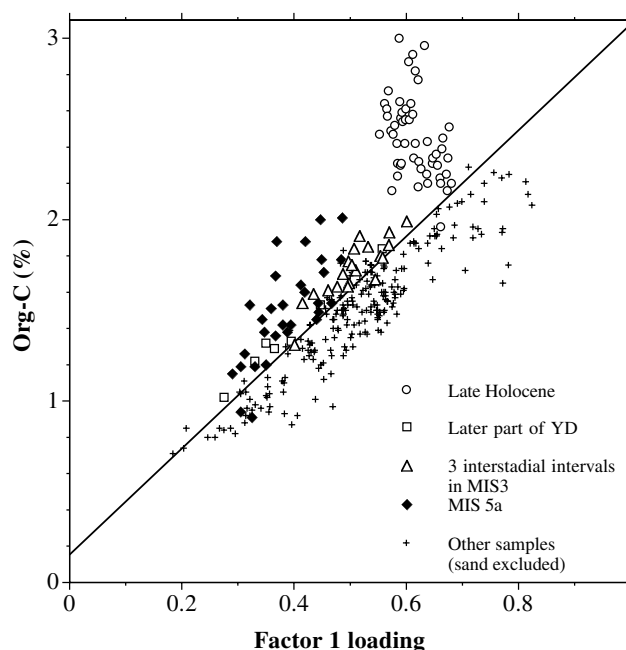


Figure 14. A diagram showing the relationship between factor 1 loading and org-C for samples from the top 15 m of Hole 1017E. The samples from six stratigraphic intervals that scatter the larger org-C side of the regression line are indicated by different symbols.

or enhanced surface productivity around 11, 43, 48, 55, and 72–81 ka. Carbonate preservation and/or productivity effects are represented by higher factor 3 loading. Factor 3 loading shows positive peaks approximately at 10, 25, 47, and 77 ka.

ACKNOWLEDGMENTS

We express our special thanks to Drs. I. Koizumi and M. Lyle for their encouragement and support throughout the course of this study. We also express our sincere thanks to staff of ODP Leg 167 cruise and of the ODP Gulf Coast Repository for their assistance with sampling and data collection. Thanks also go to Mr. Takayama for his assistance in the laboratory and Dr. R. Behl for his discussion. This study is partly supported by the Grant-in-Aid for Scientific Research of the Ministry of Education, Science and Culture of Japan No. 08458141.

REFERENCES

- Behl, R.J., and Kennett, J.P., 1996. Brief interstadial events in the Santa Barbara Basin, NE Pacific, during the last 60 kyr. *Nature*, 379:243–246.
- Berner, R.A., 1970. Sedimentary pyrite formation. *Am. J. Sci.*, 268:1–23.
- , 1984. Sedimentary pyrite formation: an update. *Geochim. Cosmochim. Acta*, 48:605–615.
- Berner, R.A., and Raiswell, R., 1983. Burial of organic carbon and pyrite sulfur in sediments over Phanerozoic time: a new theory. *Geochim. Cosmochim. Acta*, 47:855–862.
- Broecker, W.S., Lao, Y., Klas, M., and Clark, E., 1993. A search for early Holocene CaCO_3 preservation event. *Paleoceanography*, 8:333–339.
- Calvert, S.E., and Karl, R.E., 1991. Relationships between sulphur, organic carbon, and iron in modern sediments of the Black Sea. *Geochim. Cosmochim. Acta*, 55:2483–2490.
- Canfield, D.E., 1994. Factors influencing organic carbon preservation in marine sediments. *Chem. Geol.*, 114:315–329.
- Dansgaard, W., Johnsen, S.J., Clausen, H.B., Dahl-Jensen, D., Gundestrup, N.S., Hammer, C.U., Hvidberg, C.S., Steffensen, J.P., Sveinbjörnsdóttir, A.E., Jouzel, J., and Bond, G., 1993. Evidence for general instability of past climate from a 250-kyr ice-core record. *Nature*, 364:218–220.

- DeMaison, G.L., and Moore, G.T., 1980. Anoxic marine environments and oil source bed genesis. *AAPG Bull.*, 64:1179–1209.
- Gardner, J.V., and Dartnell, P., 1995. Centennial-scale late Quaternary stratigraphies of carbonate and organic carbon from Santa Barbara Basin, Hole 893A, and their paleoceanographic significance. In Kennett, J.P., Baldauf, J.G., and Lyle, M. (Eds.), *Proc. ODP, Sci. Results*, 146 (Pt. 2): College Station, TX (Ocean Drilling Program), 103–124.
- Gardner, J.V., Dean, W.E., and Dartnell, P., 1997. Biogenic sedimentation beneath the California Current system for the past 30 kyr and its paleoceanographic significance. *Paleoceanography*, 12:207–227.
- Gonopolski, A., Rahmstorf, S., Petoukhov, V., and Claussen, M., 1998. Simulation of modern and glacial climates with a coupled global model of intermediate complexity. *Nature*, 391:351–356.
- Hickey, B.M., 1979. The California Current System: hypotheses and facts. *Prog. Oceanogr.*, 8:191–279.
- Imbrie, J., and van Andel, T.H., 1964. Vector analysis of heavy-mineral data. *Geol. Soc. Am. Bull.*, 75:1131–1156.
- Irino, T., and Tada, R., 2000. Quantification of aeolian dust (Kosa) contribution to the Japan Sea sediments and its variation during the last 200 k.y. *Geochem. J.*, 34:59–93.
- Keigwin, L.D., 1998. Glacial-age hydrology of the far northwest Pacific. *Paleoceanography*, 13:323–339.
- Keil, R.G., Tsamakis, E., Fuh, C.B., Giddings, C., and Hedges, J.I., 1994. Mineralogical and textural controls on organic composition of coastal marine sediments: hydrodynamic separation using SPLITT-fractionation. *Geochim. Cosmochim. Acta*, 57:879–893.
- Kennett, J.P., and Ingram, B.L., 1995. A 20,000-year record of ocean circulation and climate change from the Santa Barbara Basin. *Nature*, 377:510–512.
- Leinen, M., and Pisias, N., 1984. An objective technique for determining end-member compositions and for partitioning sediments according to their sources. *Geochim. Cosmochim. Acta*, 48:47–62.
- Lund, D.C., and Mix, A.C., 1998. Millennial-scale deep-water oscillations: reflections of the North Atlantic in the deep Pacific from 10 to 60 Ka. *Paleoceanography*, 13:10–19.
- Lyle, M., Zahn, R., Prah, F., Dymond, J., Collier, R., Pisias, N., and Suess, E., 1992. Paleoproductivity and carbon burial across the California Current: the Multitracers Transect, 42°N. *Paleoceanography*, 7:251–272.
- Martinson, D.G., Pisias, N.G., Hays, J.D., Imbrie, J., Moore, T.C., Jr., and Shackleton, N.J., 1987. Age dating and the orbital theory of the ice ages: development of a high-resolution 0 to 300,000-year chronostratigraphy. *Quat. Res.*, 27:1–29.
- Mehra, O.P., and Jackson, M.L., 1960. Iron oxide removal from soils and clays by a dithionite-citrate system buffered with sodium bicarbonate. *Clays Clay Miner., Proc. Conf.*, 7:317–327.
- Miesch, A.T., 1976. Q-mode factor analysis of geochemical and petrologic data matrices with constant row-sums. *Geol. Surv. Prof. Pap. U.S.*, 574–G.
- Mullins, H.T., Thompson, J.B., McDougall, K., and Vercoutere, T.L., 1985. Oxygen-minimum zone edge effects: evidence from the Central California coastal upwelling system. *Geology*, 13:491–494.
- Odin, G.S., and Matter, A., 1981. Die glauconarium origine. *Sedimentology*, 28:611–643.
- Rea, D.K., and Janecek, T.R., 1981. Mass-accumulation rates of the non-authigenic inorganic crystalline (colian) component of deep-sea sediments from the western mid-Pacific Mountains, Deep Sea Drilling Project Site 463. In Theide, J., Vallier, T.L., et al., *Init. Repts. DSDP*, 62: Washington (U.S. Govt. Printing Office), 653–659.
- Savrda, C.E., Bottjer, D.J., and Gorsline, D.S., 1984. Development of a comprehensive oxygen-deficient marine biofacies model: evidence from Santa Monica, San Pedro and Santa Barbara basins, California Continental Borderland. *AAPG Bull.*, 68:1179–1192.
- Tada, R., Irino, T., and Koizumi, I., 1999. Land-ocean linkages over orbital and millennial time-scales recorded in late Quaternary sediments of the Japan Sea. *Paleoceanography*, 14:236–247.
- Tada, R., Koizumi, I., Cramp, A., and Rahman, A., 1992. Correlation of dark and light layers, and the origin of their cyclicity in the Quaternary sediments from the Japan Sea. In Pisciotto, K.A., Ingle, J.C., Jr., von Breyman, M.T., Barron, J., et al., *Proc. ODP, Sci. Results*, 127/128 (Pt. 1): College Station, TX (Ocean Drilling Program), 577–601.
- van Geen, A., Fairbanks, R.G., Dartnell, P., McGann, M., Gardner, J.V., and Kashgarian, M., 1996. Ventilation changes in the northeast Pacific during the last deglaciation. *Paleoceanography*, 11:519–528.
- Weber, M.E., Bonani, G., and Futterer, K.D., 1994. Sedimentation processes within channel-ridge systems, southeastern Weddell Sea, Antarctica. *Paleoceanography*, 9:1027–1048.

Date of initial receipt: 16 October 1998

Date of acceptance: 27 April 1999

Ms 167SR-222

Appendix A.

Organic and carbonate carbon contents and mineral composition (peak heights) of samples from Cores 167-1017E-1H and 2H.

Number	Core, section, interval (cm)	Corrected depth (mbsf)	C _{org} (%)	C _{carb} (%)	Smectite (cps)	Illite (cps)	Chlorite					
							Kaolinite (cps)	Quartz (cps)	Feldspar (cps)	Calcite (cps)	Pyrite (cps)	Amorphous hump
167-1017E-												
1	1H-1, 0-3	0.01	2.96	0.77	36	57	34	2,667	775	570	0	77,233
2	1H-1, 3-6	0.04	2.91	0.82	50	55	37	2,602	904	552	0	77,367
3	1H-1, 6-9	0.07	3.00	0.69	37	90	34	2,802	1122	619	35	76,757
4	1H-1, 9-12	0.10	2.82	0.83	40	71	41	2,707	832	591	44	77,893
5	1H-1, 12-15	0.13	2.59	0.90	35	57	36	2,668	881	586	40	68,348
6	1H-1, 15-18	0.16	2.87	0.93	49	114	43	2,725	1348	621	70	76,512
7	1H-1, 18-21	0.19	2.55	1.09	39	59	42	2,687	855	531	43	73,699
8	1H-1, 21-24	0.22	2.65	0.95	42	90	41	2,669	1033	549	44	72,400
9	1H-1, 24-27	0.24	2.56	0.92	35	65	43	2,484	896	549	31	76,071
10	1H-1, 27-30	0.27	2.77	0.83	36	69	48	2,572	951	655	45	71,378

This is a sample of the table that appears on the volume CD-ROM.

Appendix B.

Major element composition of samples from Cores 167-1017E-1H and 2H.

Number	Core, section, interval (cm)	Corrected depth (mbsf)	Major element composition (%)										
			LOI	SiO ₂	TiO ₂	Al ₂ O ₃	Fe ₂ O ₃	MnO	MgO	CaO	Na ₂ O	K ₂ O	P ₂ O ₅
167-1017E-													
1	1H-1, 0-3	0.01	11.44	57.12	0.63	12.87	4.50	0.035	2.35	5.37	2.22	2.45	0.27
2	1H-1, 3-6	0.04	11.29	57.42	0.63	12.84	4.48	0.036	2.33	5.24	2.29	2.45	0.27
3	1H-1, 6-9	0.07	11.17	57.35	0.63	12.83	4.37	0.036	2.28	5.23	2.33	2.50	0.26
4	1H-1, 9-12	0.10	11.47	57.34	0.63	12.70	4.36	0.036	2.28	5.45	2.20	2.47	0.26
5	1H-1, 12-15	0.13	12.25	57.06	0.61	12.49	4.10	0.035	2.15	5.17	2.30	2.47	0.26
6	1H-1, 15-18	0.16	11.29	57.38	0.63	12.70	4.39	0.036	2.26	5.66	2.31	2.44	0.26
7	1H-1, 18-21	0.19	11.15	57.36	0.63	12.85	4.37	0.036	2.28	5.52	2.32	2.48	0.26
8	1H-1, 21-24	0.22	11.01	57.36	0.64	12.99	4.42	0.036	2.33	5.58	2.34	2.55	0.26
9	1H-1, 24-27	0.24	10.90	56.87	0.64	12.94	4.42	0.037	2.30	5.43	2.32	2.53	0.25
10	1H-1, 27-30	0.27	11.47	57.23	0.65	13.17	4.49	0.037	2.38	5.70	2.32	2.52	0.26

This is a sample of the table that appears on the volume CD-ROM.

Appendix C.

Volume ratios of clay, fine-silt, and coarse-silt fractions within lithogenic component and modal position of fine-silt fraction of 79 selected samples from Cores 167-1017E-1H and 2H.

Number	Core, section, interval (cm)	Corrected depth (mbsf)	Fine-silt position (mm)	Clay volume (%)	Fine-silt volume (%)	Coarse silt volume (%)
4	1H-1, 9-12	0.10	12.7	12.2	65.9	21.9
6	1H-1, 15-18	0.16	14.9	10.0	71.0	19.0
8	1H-1, 21-24	0.22	13.3	9.9	68.6	21.5
10	1H-1, 27-30	0.27	12.7	10.5	71.1	18.4
12	1H-1, 33-36	0.33	13.2	11.1	68.2	20.7
14	1H-1, 39-42	0.39	13.6	12.8	64.5	22.7
16	1H-1, 45-48	0.45	12.7	11.4	69.6	19.0
18	1H-1, 51-54	0.50	13.1	10.8	70.4	18.8
20	1H-1, 57-60	0.56	12.9	11.2	73.1	15.7
22	1H-1, 63-66	0.62	13.3	13.8	64.6	21.6

This is a sample of the table that appears on the volume CD-ROM.

Appendix D.

Loadings of factors 1 to 5 for samples from Cores 167-1017E-1H and 2H.

Number	Core, section, interval (cm)	Corrected depth (mbsf)	Factor loadings				
			Factor 1	Factor 2	Factor 3	Factor 4	Factor 5
167-1017E-							
1	1H-1, 0-3	0.01	0.63	0.41	-0.038	0.0035	-0.012
2	1H-1, 3-6	0.04	0.61	0.43	-0.033	0.0031	-0.013
3	1H-1, 6-9	0.07	0.59	0.45	-0.028	0.0021	-0.013
4	1H-1, 9-12	0.10	0.62	0.40	-0.017	0.0034	-0.007
5	1H-1, 12-15	0.13	0.59	0.41	0.015	0.0012	-0.014
6	1H-1, 15-18	0.16	0.60	0.42	-0.009	0.0019	-0.012
7	1H-1, 18-21	0.19	0.60	0.44	-0.025	0.0017	-0.014
8	1H-1, 21-24	0.22	0.59	0.46	-0.036	0.0016	-0.011
9	1H-1, 24-27	0.24	0.59	0.47	-0.045	0.0011	-0.012
10	1H-1, 27-30	0.27	0.62	0.44	-0.047	0.0016	-0.016

This is a sample of the table that appears on the volume CD-ROM.